Examination of aerosol effects on precipitation in deep convective clouds during the 1997 ARM summer experiment

Seoung Soo Lee,* [†] Leo J. Donner, Vaughan T. J. Phillips[‡] and Yi Ming

Geophysical Fluid Dynamics Laboratory, Princeton University, NJ, USA

ABSTRACT: It has been generally accepted that increasing aerosols suppress precipitation. The aerosol-induced precipitation suppression was suggested by the study of shallow stratiform clouds. Recent studies of convective clouds showed increasing aerosols could increase precipitation. Those studies showed that intense feedbacks between aerosols and cloud dynamics led to increased precipitation in some cases of convective clouds. This study expanded those studies by analyzing detailed microphysical and dynamical modifications by aerosols leading to increased precipitation. This study focused on three observed cases of mesoscale cloud ensemble (MCE) driven by deep convective clouds, since MCE accounts for a large proportion of the Earth's precipitation and the study of aerosol effects on MCE is at its incipient stage. Those MCEs were observed during the 1997 Atmospheric Radiation Measurement (ARM) summer experiment. Two numerical experiments were performed for each of the MCEs to simulate aerosol effects on deep convection. The first was with high aerosol number concentration, and the second was with low concentration. The results showed an increased precipitation at high aerosol, due to stronger, more numerous updraughts, initiated by stronger convergence lines at the surface in convective regions of the MCE. The stronger convergence lines were triggered by increased evaporation of cloud liquid in the high-aerosol case, made possible by higher values of cloud liquid necessary for autoconversion.

The generality of these results requires further investigation. However, they demonstrate that the response of precipitation to increased aerosols in deep convection can be different from that in shallow cloud systems, at least for the cases studied here. Copyright © 2008 Royal Meteorological Society

KEY WORDS   microphysics; cloud condensation nuclei; mesoscale cloud ensemble

Received 20 March 2007; Revised 16 May 2008; Accepted 10 June 2008

1. Introduction

Increasing aerosols with industrialization are known to change cloud microphysics. Increasing aerosols decrease droplet size and increase cloud albedo (first aerosol indirect effect). Decreasing droplet size also lowers collection efficiencies among droplets, delaying the formation of drizzle or rain (second aerosol indirect effect). This increases the amount of low-level cloudiness through a reduction in precipitation and thus may have a significant impact on the water mass budget of clouds, their persistence, albedo and perhaps climate.

Recent studies by Khain *et al.* (2003) and van den Heever and Cotton (2004) showed that increases of the number concentration of aerosol and subsequently of cloud condensation nuclei (CCN) led to increased precipitation for deep convection, contrary to precipitation suppression proposed by Albrecht (1989) for stratiform clouds. Khain *et al.* (2003) adopted a convective case for

their simulation from the Global Atmospheric Research Programme Atlantic Tropical Experiment (GATE) and the preliminary regional experiment for the Stormscale Operational and Research Meteorology program (PRE-STORM). They showed the number concentration of typical continental aerosol produced higher cumulative rain because of the development of stronger secondary clouds, leading to the formation of stationary squall lines. The lower concentration from maritime aerosols did not develop squall lines and produced less precipitation. Both cases are characterized by unstable environments which supported deep convection and led to the formation of squall lines. van den Heever and Cotton's (2004) simulations showed invigoration of deep convective clouds in Florida due to increased ice nuclei (IN) from Saharan dust.

Khain *et al.* (2005) found that with higher aerosol number concentration, stronger convergence at the surface, induced by greater evaporation, played an important role in the formation of the stronger secondary clouds. The development of stronger secondary clouds with continental aerosol was also found in Lynn *et al.*'s (2005a,b) three-dimensional (3D) regional model with spectral microphysics. Lynn *et al.* (2005a,b) simulated squall lines over Florida and off the west coast of Florida and found heavier precipitation with higher aerosols

* Correspondence to: Seoung Soo Lee, 2455 Hayward Street, Room 1215 SRB, Ann Arbor, HI 48 109, USA. E-mail: seoungl@umich.edu
† Currently at *Department of Atmospheric, Oceanic, and Space Science, University of Michigan, Ann Arbor, MI, USA.*
‡ Currently at *Department of Meteorology, University of Hawaii, Manoa, HI, USA.*

via stronger secondary clouds. Albrecht (1989) suggested precipitation suppression for stratiform clouds, from which the deep convection simulated by Khain *et al.* (2003, 2005), van den Heever and Cotton (2004) and Lynn *et al.* (2005a,b) differed greatly in initial organization and subsequent development. These studies indicate that the role of the aerosol number concentration may be different for stratiform clouds and deep convection. Precipitation suppression may not apply to deep convection. The possibly different roles of aerosol in deep convective and stratiform clouds have also been documented where aerosol did not serve as CCN, but as a radiation absorber. Wang (2004) simulated the enhancement of convective precipitation in the northern portion of the InterTropical Convergence Zone (ITCZ) due to the existence of black carbon (BC). His result is in contrast to that of Hansen *et al.* (1997), who showed radiative heating associated with absorption of solar radiation by BC could stabilize the atmosphere to suppress precipitation of large-scale cloud systems (known as semidirect effect of aerosol).

The aim of the present paper is to investigate the hypothesis that increasing aerosol increases precipitation in deep convection via strong near-surface convergence induced by evaporation, as simulated by Khain *et al.* (2005) and Lynn *et al.* (2005a,b).

Mesescale cloud ensembles (MCEs) account for a large proportion of the Earth's precipitation, and hence they are important from a climatological standpoint (Houze, 1993). However, study of aerosol effects on MCEs is in its infancy. Thus, this study considers a MCE composed of deep convective and stratiform clouds, which lasted one day. Aerosol effects on a mesoscale cloud ensemble are a combination of different aerosol effects on deep convection and shallow stratiform clouds.

This study uses a cloud-system resolving model (CSRM) coupled with bulk microphysics based on Phillips *et al.*'s (2007a) double-moment scheme. This scheme predicts number as well as mass of cloud particles. Hence, sizes of cloud particles are allowed to be predicted. A larger model domain and longer time integration are required for the study of mesoscale systems. Bin-resolving schemes are able to explicitly calculate the particle size distribution and thus simulate clouds with better confidence than with bulk schemes. However, bulk microphysics schemes remain a viable approach for the simulation of mesoscale systems due to significantly higher computational cost associated with bin schemes. In addition, Saleeby and Cotton (2004) and Grabowski (2006) pointed out that there were still unresolved issues associated with processes such as droplet nucleation and the impact of entrainment and mixing on cloud droplet spectra for the application of bin schemes to relatively coarse resolutions used for mesoscale studies.

Sets of two experiments are conducted for the ARM case using the Weather Research and Forecasting (WRF) model coupled with double-moment microphysics. The first experiment uses predicted aerosol profiles from Geophysical Fluid Dynamics Laboratory (GFDL) global

Atmosphere Model (AM2) and is referred to as the 'high-aerosol run' henceforth. The second experiment, referred to as the 'low-aerosol run', uses aerosol profiles where aerosol mass is reduced by a factor of 10 relative to that in the high-aerosol run. The comparison of the high- and low-aerosol runs identifies how increasing aerosol number concentration due to increasing aerosol mass affects the development and precipitation of the MCE.

Khain *et al.* (2005) and Lynn *et al.*'s (2005a,b) analysis only focused on changes in mass of hydrometeors and not on detailed microphysical and dynamical modifications by aerosol leading to larger precipitation. This study expands Khain *et al.* and Lynn *et al.*'s analysis by examining the microphysical terms of the precipitation budget and dynamical terms associated with near-surface convergence, to identify processes by which aerosol number concentration affects dynamics, hydrometeor mass and precipitation.

2. Cloud-system resolving model

2.1. Dynamics and turbulence

For numerical experiments, WRF (Skamarock *et al.*, 2005) is used as a 2D non-hydrostatic compressible model. The detailed equations of the dynamical core of WRF are described by Klemp *et al.* (2007).

Hong and Pan's (1996) scheme, which includes non-gradient flux for heat and moisture and calculates vertical eddy diffusion, is used for the planetary boundary layer. For vertical diffusion in the free troposphere, Hong *et al.*'s (2006) scheme, where diffusion is represented with an implicit local scheme based on the local Richardson number, is used. The version of WRF used in these experiments uses a turbulence kinetic energy (TKE) closure. Horizontal eddy diffusion is a function of TKE, following Skamarock *et al.* (2005).

2.2. Microphysics and radiation

To represent microphysical processes, the WRF adopts Phillips *et al.*'s (2007a) double-moment bulk representation. The size distribution of cloud liquid and cloud ice ($x = $ c, i) obeys a gamma distribution:

$$n(D_x) = n_{x,0} D_x^{p_x} \exp(-\lambda_x D_x), \qquad (1)$$

where D_x is the equivalent spherical diameter (m) and $n(D_x)\mathrm{d}D_x$ is the number concentration (m^{-3}) of particles in the size range $\mathrm{d}D_x$. Also λ_x (m^{-1}) is the slope, $n_{x,0}$ is the intercept ($\mathrm{m}^{-(4+p_x)}$), and p_x is the shape parameter of the distribution.

$$\lambda_x = \left(\frac{\Gamma(4+p_x)\rho_x \frac{\pi}{6} n_x}{\Gamma(1+p_x)q_x} \right)^{\frac{1}{3}} \quad \text{and}$$

$$n_{x,0} = \frac{(n_x \rho_a)\lambda_x^{1+p_x}}{\Gamma(1+p_x)}.$$

Here, Γ is the Gamma function, ρ_x and n_x are the particle bulk density (kg m^{-3}) and number mixing ratio (particle number per unit air mass; kg^{-1}), respectively. ρ_a is the air density. For ice particles, a bulk density close to that of pure ice is assumed ($\rho_i = 900$ kg m^{-3}). p_i and p_c are set to unity and 3.5, respectively, based on field experiments described in Phillips *et al.* (2007a).

Droplet nucleation follows Ming *et al.*'s (2006) nucleation parametrization. In their parametrization, aerosol can take any form of size distribution and chemical composition. Critical supersaturation, S_c, and critical radius, r_c, are calculated considering aerosol chemical composition, based on the Köhler theory. For surface tension depression by dissolved organic substances, Facchini *et al.*'s (1999) measured suppression is used. Maximum supersaturation, $S_{\max}$, of a closed adiabatic parcel is calculated based on the equation of supersaturation prediction from Leaitch *et al.* (1986) for primary nucleation, occurring in cloud-free air; the supersaturation in the parcel increases with increasing vertical positive velocity of updraughts and decreases with increasing condensation. When the increase exactly counterbalances the decrease, the supersaturation is at its equilibrium where supersaturation becomes $S_{\max}$. $S_{\max}$ is obtained by solving Leaitch *et al.*'s equation of supersaturation prediction numerically. $S_{\max}$ for secondary nucleation (in-cloud nucleation) is obtained from Phillips *et al.*'s (2007a) linearized supersaturation scheme. Aerosols whose S_c is lower than $S_{\max}$ are counted as nucleated droplets in Ming *et al.*'s (2006) parametrization.

Lohmann and Diehl's (2006) parametrizations, taking into account the dependence of IN activation on dust and BC aerosol mass, are used for contact, immersion, and condensation-freezing activation of IN. For contact activation:

$$\frac{dN_{cnt}}{dt} = m_{io} D_{ap} 4\pi r_{cm} N_{a,cnt} \frac{\rho_a n_c^2}{q_c}, \qquad (2)$$

where dN_{cnt}/dt (m^{-3}s^{-1}) is the rate of ice-crystal number production via contact freezing, m_{io} (10^{-12} kg) is the original mass of a newly formed ice crystal, D_{ap} (m^2 s^{-1}) is the Brownian aerosol diffusivity, r_{cm} is volume-mean droplet radius, $N_{a,cnt}$(m^{-3}) is the number concentration of contact nuclei and n_c is the number mixing ratio of droplets. $N_{a,cnt}$ is obtained from the number of aerosol particles consisting of BC and dust, multiplied by a species-specific temperature dependence. For dust, temperature dependence of montmorillonite is adopted (Lohmann and Diehl, 2006). For immersion and condensation-freezing activation:

$$\frac{dN_{imm}}{dt} = N_{a,imm} \exp(T_0 - T)\frac{dT}{dt}\frac{\rho_a q_c}{\rho_w}, \qquad (3)$$

where dN_{imm}/dt (m^{-3}s^{-1}) is the rate of ice-crystal number production via immersion and condensation freezing, and T_0 is the freezing temperature. $N_{a,imm}$ (m^{-3}) is the number concentration of immersion and condensation

nuclei, calculated as the number of BC and dust aerosols, multiplied by a temperature dependence for immersion and condensation freezing. ρ_w is the water density. As for contact freezing, temperature dependence of montmorillonite is adopted for dust. For deposition nucleation, Möhler *et al.*'s (2006) parametrization, calculating the fraction of dust activated, is implemented:

$$\frac{dN_{dep}}{dt} = N_{a,dep}[\exp\{a(S_i - S_0)\} - 1], \qquad (4)$$

where dN_{dep}/dt (m^{-3}s^{-1}) is the rate of ice-crystal number production via depositional freezing, a and S_0 are non-dimensional empirical constants determined by chamber experiments. Here a and S_0 are set to 4.77 and 1.07, respectively, based on experiments for desert dust. $N_{a,dep}$ is the number concentration of deposition nuclei (m^{-3}) calculated from predicted total dust mass. (4) is applied at temperatures lower than $-40\,^\circ$C and restricted to $S_0 < S_i < 1.63 + 6.52 \times 10^{-3} \times (T - T_0)$, corresponding to Field *et al.*'s (2006) measured saturation region where pure deposition nucleation occurs. The parametrization is limited to activating a maximum of 5% of the dust, following Field *et al.*'s (2006) measurements. As indicated by Field *et al.*'s (2006) experiments, (4) is only valid at temperatures below $-40\,^\circ$C. At temperatures higher than $-40\,^\circ$C, Meyers *et al.* (1992) and DeMott *et al.*'s (2003) parametrizations, multiplied by a scaling factor to consider the dependence of IN activation on dust mass, are used. Those parametrizations are applied to grid points with no cloud liquid to ensure only deposition nucleation is calculated. It is limited to activating a maximum of 0.5% of the dust, since Field *et al.* (2006) found deposition nucleation did not activate more than 0.5% of the dust at temperatures higher than $-40\,^\circ$C. Details of those parametrizations can be found in the appendix.

For radiation, a simplified version of the GFDL radiation code is incorporated into WRF (Freidenreich and Ramaswamy, 1999; Schwarzkopf and Ramaswamy, 1999). The radiative effects of cloud liquid, cloud ice, rain, snow, graupel, water vapour, CO_2 and O_3 are included. Effective sizes of cloud liquid and cloud ice are predicted using assumed size distributions. A generalized effective size of cloud ice is inferred from the mean size of the equivalent spherical diameter following Phillips *et al.* (2007a).

3. Integration design

Houze (1993) defined a mesoscale convective system as a cloud system that occurs in connection with an ensemble of thunderstorms and produces precipitation area $\sim$100 km or more in horizontal scale in at least one direction. The model domain has two dimensions. The horizontal and vertical domains are 168 km and 20 km, respectively, to cover a mesoscale cloud system. The horizontal grid length is 2 km and the vertical grid length is 500 m. Arakawa C-grid staggering is used.

Periodic boundary conditions are set on horizontal boundaries, and heat and moisture fluxes are prescribed at the surface. To prevent the reflection of gravity or sound waves from the model top, a damping layer of 5 km depth is applied near the model top.

ARM sub-case A observations provide large-scale forcing. Balloon soundings of winds, temperature and dew-point temperature were obtained every 3 hours from the ARM SGP clouds and radiation testbed (CART) central facility located near Lamont, Oklahoma (36.61 °N, 97.49 °W) and from four boundary facilities. Sub-case A produced the largest precipitation rate among the 1997 IOP sub-cases through development of a deep convective MCE. The sounding/profiler data, combined with the surface and the top-of-the-atmosphere flux observations, were analyzed using a constrained variational objective analysis method by Zhang and Lin (1997) and Zhang *et al.* (2001). The 3-hourly analyses were applied to the model as the large-scale advection for potential temperature and specific humidity at every time step by interpolation. Temperature and humidity were also nudged toward observations with a relaxation time of one hour. The model domain is considered to be small compared to large-scale disturbances. Hence, the large-scale advection is approximated to be uniform over the model domain and large-scale terms are defined to be functions of height and time only, following Krueger *et al.* (1999). Identical observed surface fluxes of heat and moisture were prescribed in both high- and low-aerosol runs using the Energy Balance Bowen Ratio (EBBR) station measurement at the SGP site. This method of modelling cloud systems was used for the CSRM comparison study by Xu *et al.* (2002). The CSRMs in the comparison study could reasonably simulate midlatitude continental summer convection observed at the ARM CART site in terms of convective intensity, temperature and specific humidity evolution. The details of the procedure for applying large-scale forcing are described in Donner *et al.* (1999) and are similar to the method proposed by Grabowski *et al.* (1996). Horizontal momentum was damped to observed values, following Xu *et al.* (2002).

Convection in the model is initiated by imposing perturbations on the initial water vapour mixing ratio at the first time step. The perturbations vary in the horizontal but are constant throughout the lowest 1.5 km in each column of the model. The perturbations are horizontally random, generated from a uniform distribution between ± 2 g kg^{-1}. These perturbations are similar to those employed by Donner *et al.* (1999) and are chosen to be random so as not to impose organized structure on the convection when it develops.

The aerosol profiles for these simulations were extracted from a version of the GFDL AM2 (2004) nudged by National Ceners for Environmental Prediction (NCEP) reanalysis with aerosol chemistry. The details of procedure for nudging NCEP reanalysis are similar to Timmreck and Schulz (2004). Aerosol chemistry is adopted from Chin *et al.* (2002) and Koch and

Rind (1998). Chemical reactions include dimethylsulphide (DMS) oxidation by OH during the day and by NO_3 during the night to form SO_2, and SO_2 oxidation by OH in the gas phase and by H_2O_2 in the aqueous phase to form sulphate. The predicted mass profiles, averaged over a one-day period, are obtained at (36.61 °N, 97.49 °W) on 26 June 1997. The vertical profiles shown in Figure 1 are used for high-aerosol experiments. Low-aerosol experiments are conducted with aerosol profiles obtained by reducing these aerosol mass concentrations by a factor of 10. Sulphate, organic and salt aerosols are assumed to act only as CCN and to have tri-modal log-normal size distributions. The mode diameter and standard deviation of the distributions, as well as the partitioning among modes, are assumed to follow Whitby's (1978) values for clean continental air mass and not to vary spatio-temporally. Dust and BC aerosols are assumed to act only as IN with uni-modal log-normal size distributions. For BC and dust, mode diameter and standard deviation are from Seinfeld and Pandis's (1998) values for remote continental areas. As assumed for aerosols acting as CCN, mode diameter and standard deviation are assumed not to vary for those acting as IN. For the assumed log-normal size distribution with the constant standard deviation and mode radius here, the ratio of aerosol mass partitioned into each size bin of the distribution to total aerosol mass does not vary with total aerosol mass. Hence, decreased total aerosol mass by a factor of 10 leads to 10-fold decreases in the partitioned aerosol mass in all size bins in the low-aerosol experiments. This also leads to 10-fold decreases in aerosol number in each bin of the size distribution, since the identical particle density of each aerosol species is used for the high- and low-aerosol experiments.

Depending on predicted mass within cloud, total aerosol number for each aerosol species varies but is reset to the background value at all levels outside cloud. Within clouds, aerosols are advected, diffused and depleted by nucleation (nucleation scavenging). Initially aerosol mass mixing ratio is everywhere set equal to its background value. Background aerosol number concentrations for all
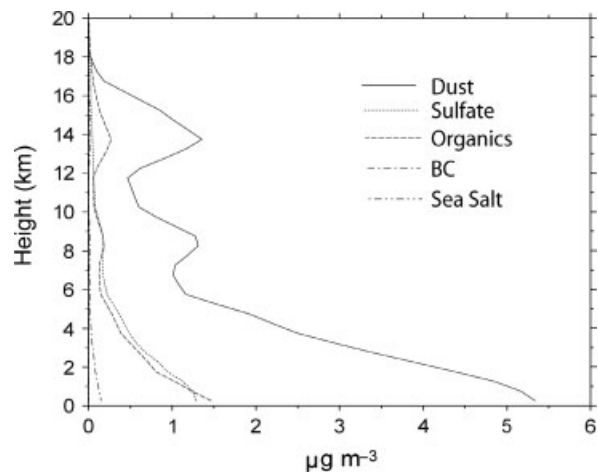

Figure 1. Vertical profiles of aerosol species for high-aerosol runs. Salt is present, but its values are less than 0.01 μg m^{-3}.

aerosol species in each aerosol size mode are assumed not to vary during time integration, since the variation of the extracted aerosols from GFDL AM2 is not significant on the date of simulations. Thus profiles averaged over a one-day period are assumed to well represent background conditions of aerosols on the date of simulations. This is equivalent to assuming no advection of unactivated aerosols into the model domain either from the surface or from outside the domain through large-scale advection.

4. Results

4.1. Precipitation rate and cumulative precipitation

Figure 2 depicts the time series of the area-mean precipitation rate smoothed over 3 hours for the entire domain for ARM sub-case A (one of the sub-cases in the 1997 IOP). The experiment using aerosol profiles from GFDL AM2 (Figure 1) is referred to as 'high-aerosol run (Exp. 1)', and the experiment using aerosol profiles whose mass is reduced by a factor of 10 is referred to as 'low-aerosol run (Exp. 2)'. The precipitation event at 2330 GMT on 29 June is driven by deep convective clouds, leading to the occurrence of the largest precipitation rate during the observation period of the sub-case A. Since the focus of this study is on identifying the mechanism leading to precipitation increases with increasing aerosols in deep convection, this precipitation event is chosen for analysis. Meteorological fields at 1130 GMT on 29 June, acting
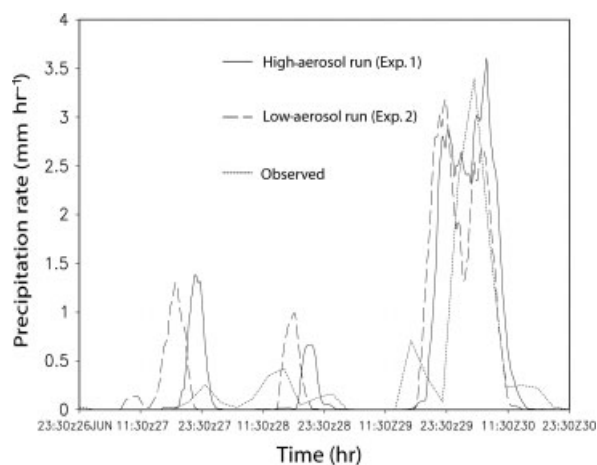

Figure 2. Time series of the areal-mean precipitation rate.

as initial conditions for the selected precipitation event, differ slightly because of different development through earlier precipitation events for Exp. 1 and Exp. 2. Differences in the subsequent cloud development would be caused not only by differences in aerosol but also by differences in meteorological fields. Hence, comparisons between Exp. 1 and Exp. 2 for the selected event would not be able to isolate aerosol effects on deep convective clouds. To isolate aerosol effects, another low-aerosol experiment (low-aerosol run, Exp. 3) is performed by adopting meteorological fields of the high-aerosol run (Exp. 1) with the same aerosol profile as in the low-aerosol run (Exp. 2) at 1130 GMT on 29 June as initial conditions; the wind, pressure, temperature, and humidity at each grid point over the whole domain from Exp. 1 are applied to the corresponding grid point in Exp. 3 at 1130 GMT on 29 June as initial conditions. Note that aerosol profiles are reset to their background values at 1130 GMT on 29 June, since there are no clouds. Most of presented comparisons are between the high-aerosol run (Exp. 1) and low-aerosol run (Exp. 3) for the precipitation event at 2330 GMT on 29 June. A fourth experiment (high-aerosol run, Exp. 4) is performed by adopting meteorological fields of the low-aerosol run (Exp. 2) with the same aerosol profile as in high-aerosol run (Exp. 1) at 1130 GMT on 29 June as initial conditions. Comparisons between the high-aerosol run (Exp. 4) and low-aerosol run (Exp. 2) are performed for the precipitation event at 2330 GMT on 29 June to examine the sensitivity of aerosol effects to initial meteorological conditions. These comparisons are presented in section 4.5. The description of simulations is given in Table I.

Maximum convective available potential energy (CAPE) of $\sim$2500 J kg^{-1} is generated and maximum wind shear is $\sim$15 m s^{-1} in simulations. The wind shear is defined as the difference between the density-weighted mean wind speed over the lowest 6 km of the profile and the average wind speed over the lowest 500 m of the profile, following the definition of Weisman and Klemp (1982). According to Bluestein's (1993) classification, this environmental condition of CAPE and shear leads to the development of cumulonimbus-type clouds, which drive the simulated MCE here.

Figure 3 shows (a) precipitation rate and (b) cumulative rainfall for the high-aerosol run (Exp. 1) and low-aerosol run (Exp. 3). Around 2130 GMT on 29 June, the precipitation rate of the high-aerosol run (Exp.

Table I. Background aerosols and meteorological conditions at 1130 GMT on 29 June for simulations.

| Simulation run	Background aerosol at 1130 GMT on 29 June	Meteorological conditions at 1130 GMT on 29 June
High aerosol (Exp. 1)	High aerosols	Determined by earlier evolution of meteorological fields with high aerosols
Low aerosol (Exp. 2)	Low aerosols (10 times smaller aerosol mass than high aerosols)	Determined by earlier evolution of meteorological fields with low aerosols
Low aerosol (Exp. 3)	Same as in low-aerosol run (Exp. 2)	Same as in high-aerosol run (Exp. 1)
High aerosol (Exp. 4)	Same as in high-aerosol run (Exp. 1)	Same as in low-aerosol run (Exp. 2)
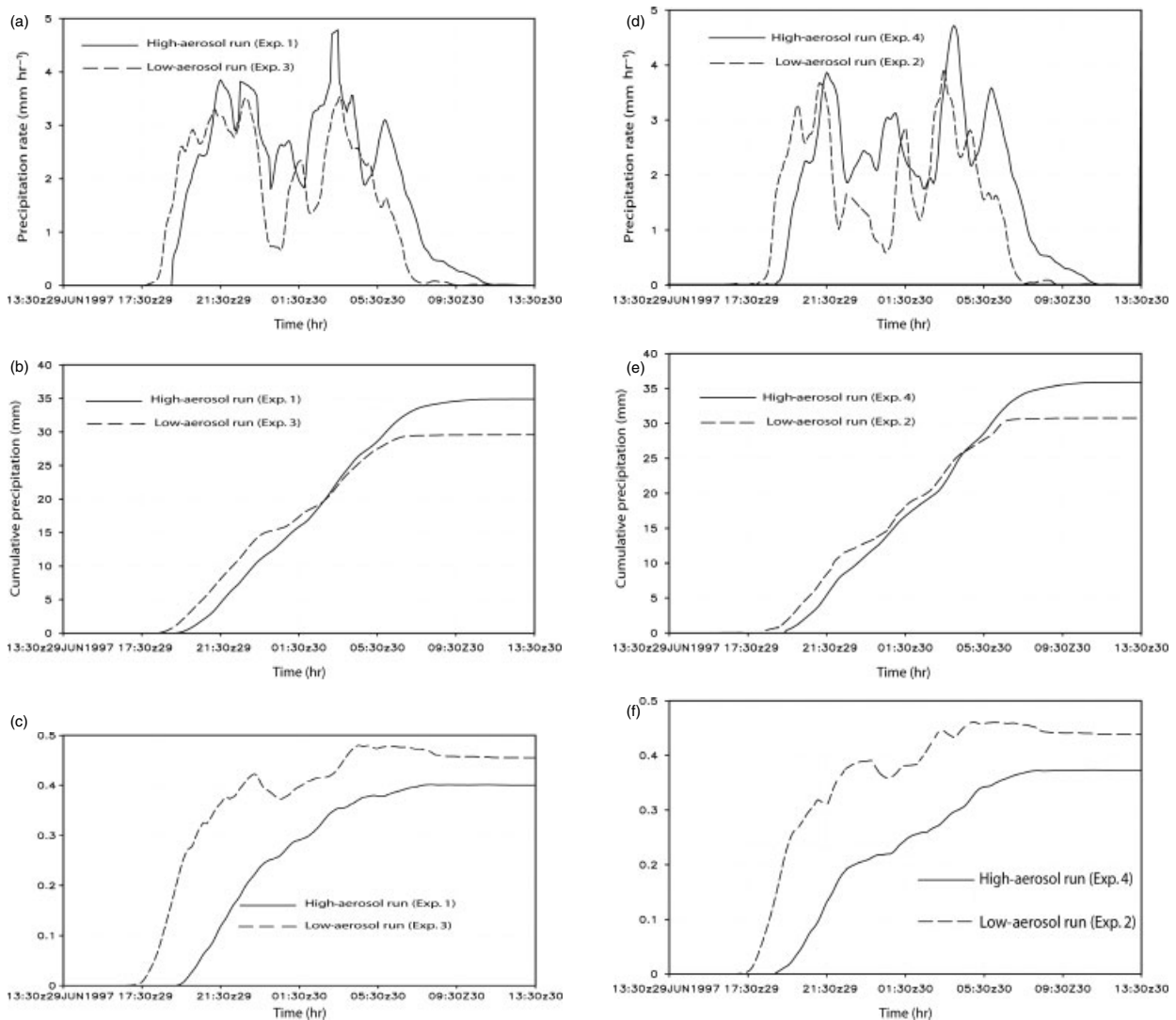
Figure 3. (a) Areal-mean precipitation rate, (b) cumulative precipitation and (c) cumulative precipitation normalized with respect to cumulative condensation for high-aerosol run (Exp. 1) and low-aerosol run (Exp. 3), starting at 1130 GMT on 29 June. (d), (e) and (f) are the same as (a), (b), and (c), respectively, but for the high-aerosol run (Exp. 4) and low-aerosol run (Exp. 2).

1) begins to exceed that of the low-aerosol run (Exp. 3). The cumulative rainfall of the high-aerosol run (Exp. 1) exceeds that of the low-aerosol run (Exp. 3) around 0230 GMT on 30 June. The domain-averaged cumulative rainfall of high-aerosol run (Exp. 1) is 34.91 mm, about 18% larger than that of the low-aerosol run (Exp. 3), at the end of the event. This increase is in marked contrast to the precipitation suppression proposed by Albrecht (1989) for shallow clouds and is plausibly a result of different interactions between dynamics and microphysics in deep and shallow cloud systems.

4.2. Precipitation budget

Microphysical processes leading to the differences in precipitation are examined by obtaining differences in domain-averaged cumulative sources and sinks of the sum of precipitable hydrometeors between the high-aerosol run (Exp. 1) and low-aerosol run (Exp. 3) (high-

aerosol − low aerosol). For this, production equations for the sum of precipitable hydrometeors are integrated over the domain and duration of the simulations (Lin *et al.*, 1983, gives production equations). The time- and domain-average tendency is zero, since the storage of the hydrometeors is zero at the end of simulation. The sources and sinks are shown in Table II, referred to as the autoconversion-accretion form of the precipitation budget. In Table II, the mixing ratios of water vapour, cloud liquid, cloud ice, rain, graupel, and snow are represented by q_v, q_c, q_i, q_r, q_g and q_s, respectively, and *Au, A, Sh, S, E, M, C, De* and *HM* represent autoconversion, accretion, shedding, sublimation, evaporation, melting, condensation, deposition, and Hallett and Mossop's (1974) rimesplintering, respectively. *Pr* is precipitation. Notation for terms in the table obeys the following conventions: the variable before the semicolon in each term indicates the quantity whose mixing ratio is changed by the source or sink. Following the semicolon, quantities that merge or

separate in the source or sink are indicated by '|' between them; a single variable following a semicolon indicates a quantity whose mixing ratio is changed by a phase transition. Volume and area integrations are denoted by $< . >$ and $\| . \|$, respectively:

$$< A > = \frac{1}{L_x} \int \int \int \rho_a A \, \mathrm{d}x\mathrm{d}z\mathrm{d}t,$$

$$\| A \| = \frac{1}{L_x} \int \int A \, \mathrm{d}x\mathrm{d}t.$$

L_x is the domain length (168 km).

Table II shows increases and decreases in precipitation resulting from compensation among terms. Sources of negative (positive) difference and sinks of positive (negative) difference contribute to less (more) rain in the high-aerosol run (Exp. 1). Among the sources and sinks, autoconversion and terms associated with accretion of cloud liquid predominantly account for precipitation differences to yield the following approximate difference

Table II. Accumulated sources and sinks of precipitation (autoconversion – accretion form), averaged over domain.

Sources and sinks of precipitation (mm): Autoconversion – Accretion form		Difference*
Sources		
$< Au(q_r; q_c|q_c) >$	Autoconversion	−17.37
$< A(q_r; q_c|q_r) >$	Accretion of cloud liquid by rain	7.99
$< A(q_g; q_c|q_g) >$	Accretion of cloud liquid by graupel	7.65
$< A(q_s; q_c|q_s) >$	Accretion of cloud liquid by snow	5.93
$< Sh(q_r; q_c|q_s) >$ $+ < Sh(q_r; q_c|q_g) >$	Shedding of cloud liquid from snow or graupel	0.76
$< A(q_g; q_i|q_g) >$	Accretion of cloud ice by graupel	0.21
$< Au(q_s; q_i|q_s) >$	Accretion of cloud ice by snow	0.25
$< Au(q_s; q_i|q_i) >$	Autoconversion of cloud ice	0.04
$< A(q_s; q_c|q_i) >$	Accretion of cloud liquid by cloud ice	0.01
$< A(q_s; q_i|q_r) >$	Accretion of cloud ice by rain to form snow	0.00
$< A(q_g; q_i|q_r) >$	Accretion of cloud ice by rain to form graupel	0.00
$< S(q_s; q_i) >$	Depositional growth of cloud ice to form snow	0.00
Sinks		
$< E(q_v; q_r) >$	Evaporation of rain	0.19
$< E(q_v; q_s) >$	Sublimation of snow	0.54
$< E(q_v; q_g) >$	Sublimation of graupel	0.20
$\|Pr\|$	Precipitation	5.32

* High-aerosol run (Exp. 1) minus low-aerosol run (Exp. 3). See text for explanation of symbols.

equation:

$$\Delta \left(< \frac{\partial q_r}{\partial t} > + < \frac{\partial q_g}{\partial t} > + < \frac{\partial q_s}{\partial t} > \right) = \Delta \| Pr \|$$

$$5.32$$

$$\approx \Delta < Au(q_r; q_c|q_c) > + \Delta < A(q_r; q_c|q_r) >$$
$$-17.37 \qquad\qquad 7.99$$
$$+ \Delta < A(q_g; q_c|q_g) > + \Delta < A(q_s; q_c|q_s) >$$
$$7.65 \qquad\qquad 5.93$$
$$+ \Delta < Sh(q_r; q_c|q_s) + Sh(q_r; q_c|q_g) >$$
$$0.76 \qquad\qquad \text{(mm)}.$$
$$(6)$$

The terms on the right-hand side of (6) are differences in autoconversion, accretion of cloud liquid by rain, accretion of cloud liquid by graupel, accretion of cloud liquid by snow, shedding of cloud liquid from snow and shedding of cloud liquid from graupel, respectively, between high- and low-aerosol runs. The sources and sinks excluded from (6) contribute ~1 order of magnitude less to the differences in precipitation than sources retained in (6).

Increased aerosols lead to increased precipitation. This is due to the increase in accretion larger than decrease in autoconversion. The presence of increased cloud liquid is required for the large increase in accretion. To examine the source of the increased cloud liquid, the terms in the budget in Table II are replaced with the terms which balance them in the liquid water budget.

The result is shown in Table III, referred to as the condensation-evaporation form of the precipitation budget. Table III shows differences in condensation and evaporation of cloud liquid are 1 to 3 orders of magnitude larger than the other terms. Therefore, the difference in precipitation is approximated as follows:

$$\Delta \| Pr \| \approx \Delta < C(q_c; q_v) > - \Delta < E(q_v; q_c) >$$
$$5.32 \qquad 22.98 \qquad 17.99 \qquad \text{(mm)}.$$
$$(7)$$

This formulation is also used in Khain *et al.* (2008). Increased condensation of cloud liquid is greater than the increased evaporation of cloud liquid, resulting in the greater high-aerosol precipitation. This leads to a drier atmosphere at high aerosol at the end of time integration, as shown in Figure 4. The greater condensation leads to larger accretion of cloud liquid by hydrometeors in the high-aerosol run (Exp. 1), as shown in (6). The greater condensation and evaporation at high aerosol are also observed in Khain *et al.* (2004) and Phillips *et al.* (2007b).

Cumulative precipitation normalized with respect to cumulative condensation at the end of time integration is 0.40 and 0.46 in the high-aerosol run (Exp. 1) and low-aerosol run (Exp. 3), respectively. Figure 3(c) shows the time series of the normalized precipitation. The low-aerosol run (Exp. 3) has higher values throughout the

Table III. Accumulated sources and sinks of precipitation (condensation – evaporation form), averaged over domain.

Sources and sinks of precipitation (mm) : Condensation – Evaporation form		Difference[*]
Sources		
$< C(q_c; q_v) >$	Condensation	**22.98**
$< A(q_g; q_i|q_g) >$	Accretion of cloud ice by graupel	0.21
$< A(q_s; q_i|q_s) >$	Accretion of cloud ice by snow	0.25
$< M(q_c; q_i) >$	Melting of cloud ice	0.02
$< Au(q_s; q_i|q_i) >$	Autoconversion of cloud ice	0.04
$< A(q_s; q_i|q_r) >$	Accretion of cloud ice by rain to form snow	0.00
$< A(q_g; q_i|q_r) >$	Accretion of cloud ice by rain to form graupel	0.00
$< De(q_s; q_i) >$	Depositional growth of cloud ice to form snow	0.00
Sinks		
$< E(q_v; q_c) >$	Evaporation of cloud liquid	**17.99**
$< F(q_i; q_c) >$	Freezing of cloud liquid	0.03
$< HM(q_i; q_c|q_s) >$ $+ < HM(q_i; q_c|q_g) >$	Rime splintering	0.01
$< E(q_v; q_r) >$	Evaporation of rain	−0.19
$< E(q_v; q_s) >$	Sublimation of snow	0.54
$< E(q_v; q_g) >$	Sublimation of graupel	−0.20
$||Pr||$	Precipitation	5.32

[*] High-aerosol run (Exp. 1) minus low-aerosol run (Exp. 3).
See text for explanation of symbols.

simulation. In spite of the lower efficiency of rain production at high aerosol, high-aerosol run (Exp. 1) produces larger cumulative precipitation. The increase in precipitation in this system is made possible by an increase in condensation which dominates the reduced efficiency with which cloud liquid is converted to precipitation. Increased condensation requires increased cooling, which can be provided by a change in the dynamics of the system between high-aerosol run (Exp. 1) and low-aerosol run (Exp. 3).

4.3. Dynamic aspects

Domain-averaged updraught mass fluxes (for those whose values are >0) below 5 km in the high-aerosol run (Exp. 1) are weaker than in the low-aerosol run (Exp. 3) around the beginning of simulation (Figure 5(a)). Around 1950 GMT on 29 June, updraughts in high-aerosol run (Exp. 1) begin to be stronger leading to higher condensation rates.

Updraughts have roots in near-surface convergence, and the intensity and areal extent of updraughts are highly correlated with the convergence. Khain *et al.*'s (2005) simulations suggest that more intense near-surface convergence may play a role in the larger precipitation
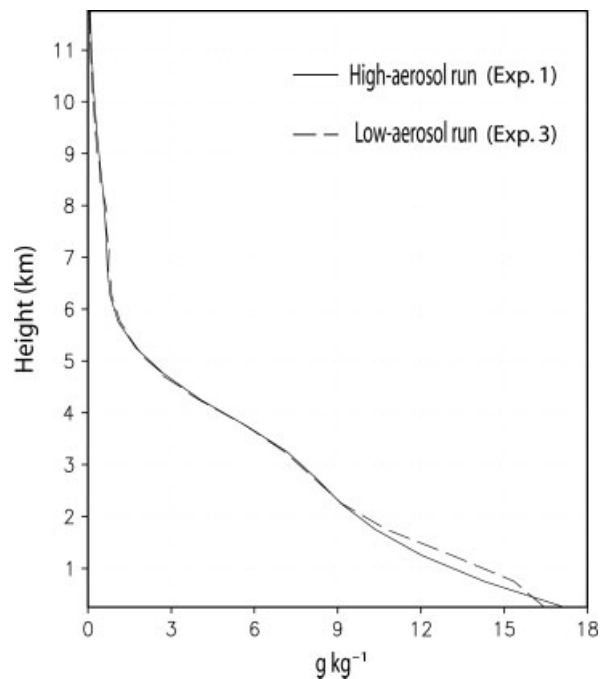

Figure 4. Vertical distribution of time-averaged water vapour mixing ratio for the high-aerosol run (Exp. 1) and low-aerosol run (Exp. 3) at the last time step.

at high aerosol. Figure 5(b) shows the time series of the average of $|\partial u/\partial x|$ over the horizontal domain and lowest 1 km, where u is horizontal wind velocity. In the high-aerosol run (Exp. 1), it begins to exceed its value in low-aerosol run (Exp. 3) at 1920 GMT on 29 June, indicating more active near-surface horizontal convergence, leading to more intense updraughts.

Figures 6(a) and (b) are the superposition of vertically averaged condensation rate and convergence at the surface at 1955 GMT on 29 June, 5 minutes after the updraught in high- aerosol run (Exp. 1) begins to be more intense than in low-aerosol run (Exp. 3). The locations of strong condensation lie over those of strong convergence, because convergence at the surface induces updraughts. Due to stronger convergence at the surface at high aerosol, more intense updraughts and active condensation take place.

The evaporation of cloud liquid or rain plays an important role in controlling the intensity of the convergence. The role of evaporation is investigated by obtaining differences in variables associated with the intensity of the convergence. Figure 7 shows the time series of the difference (high aerosol – low aerosol) in domain-averaged evaporation rate of cloud liquid and rain, condensation rate, and mass concentration of cloud liquid, updraught mass flux, the lowest 1 km downdraught mass flux and $|\partial u/\partial x|$. Around 1850 GMT, cloud liquid at high aerosol begins to be more abundant, leading to larger evaporation of cloud liquid. Delayed autoconversion in high-aerosol run (Exp. 1) due to higher cloud droplet number concentration (CDNC) results in more abundant cloud liquid at high aerosol. In-cloud average CDNCs at high aerosol and at low aerosol are 361 and
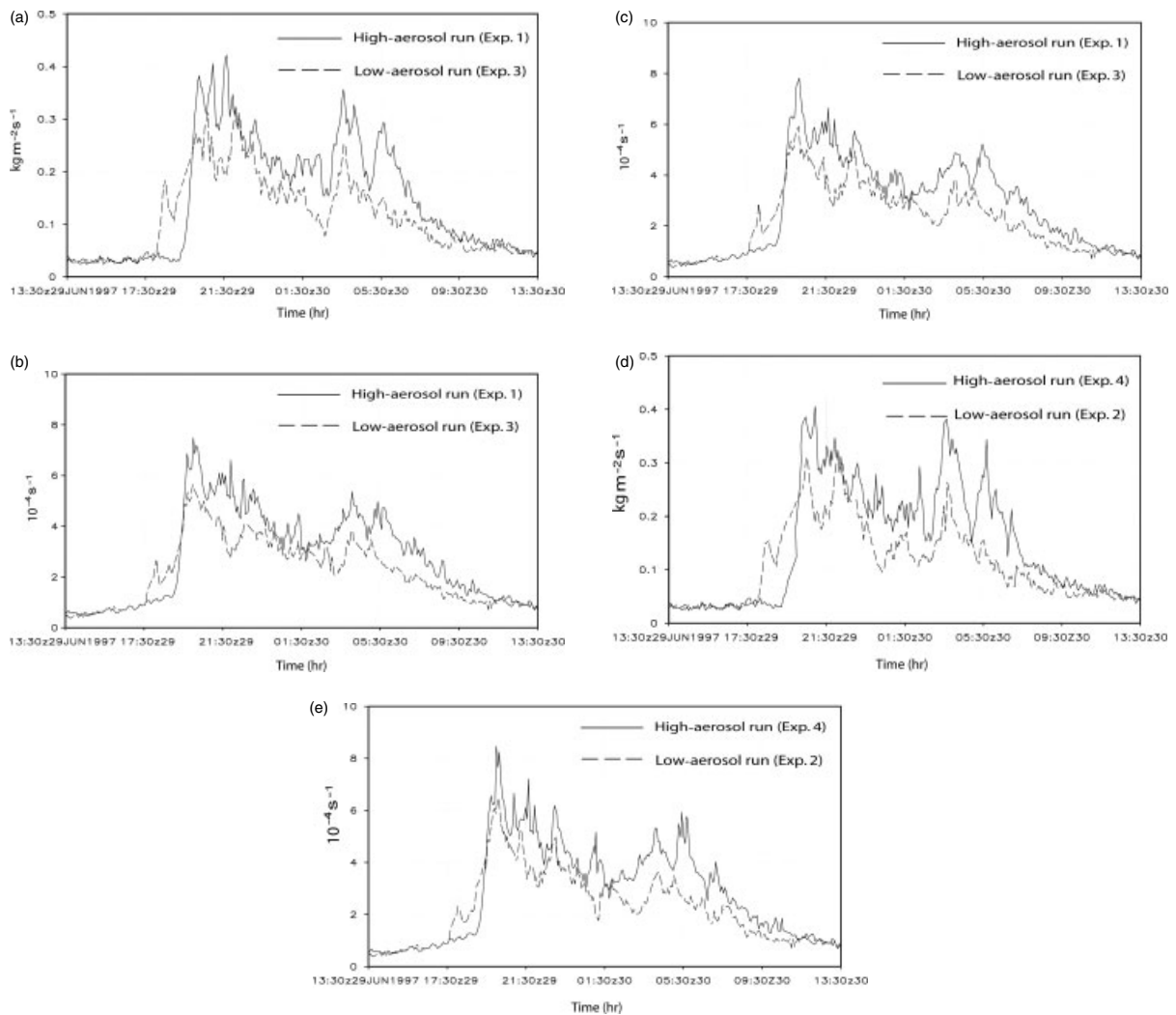
Figure 5. Time series of (a) domain-averaged updraught mass flux (for those whose values are above zero at the lowest 5 km), (b) and (c) $|\partial u/\partial x|$, averaged over horizontal domain at the lowest 1 km. (a) and (b) are for high-aerosol run (Exp. 1) and low-aerosol run (Exp. 3) and (c) is from the cases with no cold microphysics. u is the horizontal wind velocity. (d) and (e) are the same as (a) and (b), respectively, but for high-aerosol run (Exp. 4) and low-aerosol run (Exp. 2).

102 cm^{-3}, respectively. Higher CDNC provides larger surface area of droplets where water vapour condenses at high aerosol than at low aerosol. However, condensation is smaller at high aerosol due to weaker updraughts prior to ~1950 GMT. Evaporation of rain around 1850 GMT at high aerosol is lower than at low aerosol, because less rain is produced by autoconversion at high aerosol, providing less rain to unsaturated areas. Figures 8(a) and (b) show evaporation and condensation rates and wind vectors at 1915 GMT, 5 minutes before more intense low-level convergence at high aerosol develops (Figure 7). More evaporation induces stronger low-level downdraughts (averaged over the lowest 1 km) at high aerosol than at low aerosol. Stronger outflows from downdraughts around the surface intensify low-level convergence more at high aerosol, leading to more intense low-level convergence at 1920 GMT (Figure 7). Up to 1915 GMT, high-aerosol run (Exp. 1) shows substantially larger evaporative cooling than low-aerosol run (Exp. 3)

as shown in Figure 9(a). Figure 9(a) also shows most differences in evaporation between high- and low-aerosol runs are below the freezing level (~4.5 km). However, differences in cooling due to sublimation are negligible compared to those in evaporative cooling (Figure 9(b)). Figures 8(a,b) and 9 illustrate that most downdraughts develop below the freezing level due to evaporative cooling, indicating that downdraughts are controlled by evaporation in the low troposphere below the freezing level but not by evaporation and sublimation above the freezing level.

Condensation, updraughts and evaporation of rain which contribute to the development of near-surface convergence are less active at high aerosol prior to 1920 GMT when the convergence becomes more intense at high aerosol. Condensation and updraught become more active after ~1950 GMT as a result of more intense convergence at high aerosol. This time sequence, in which increased cloud liquid and evaporation at high aerosol
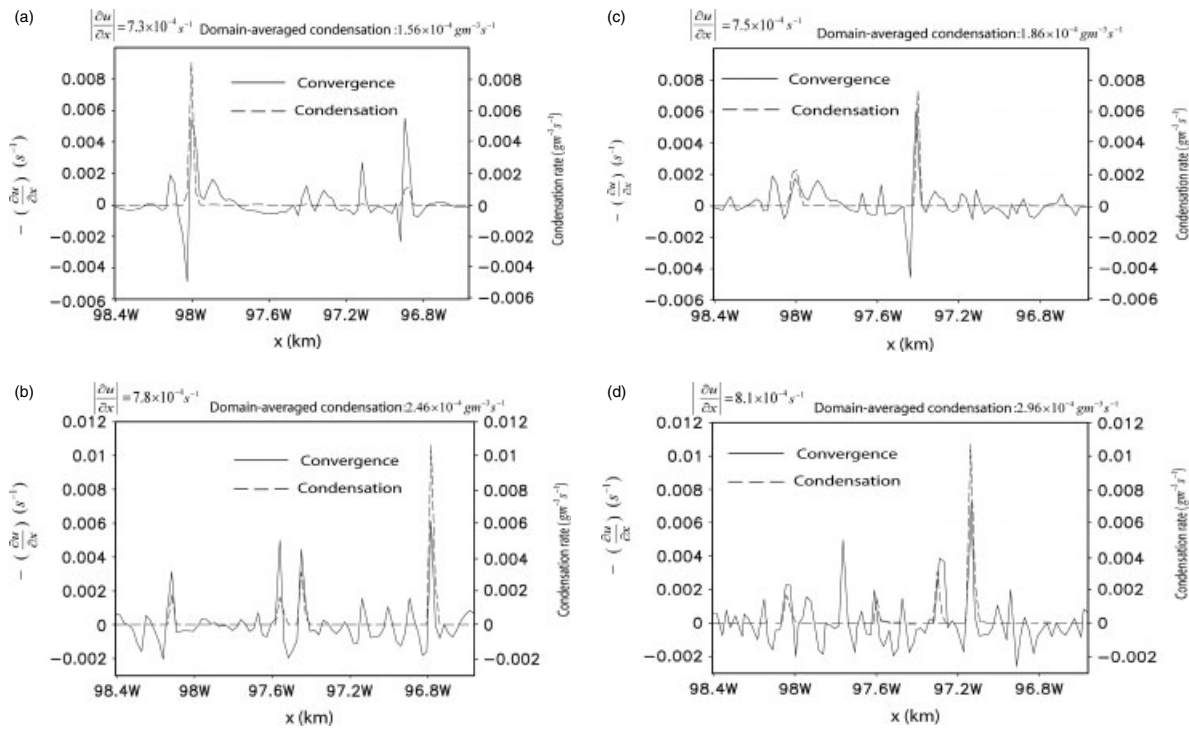
Figure 6. The superposition of vertically averaged condensation rate (g m^{-3} s^{-1}) and convergence field (s^{-1}) at the surface for (a) low-aerosol run (Exp. 3) and (b) high-aerosol run (Exp. 1), (c) low-aerosol run (Exp. 2), and (d) high-aerosol run (Exp. 4), all at 1935 GMT on 29 June.
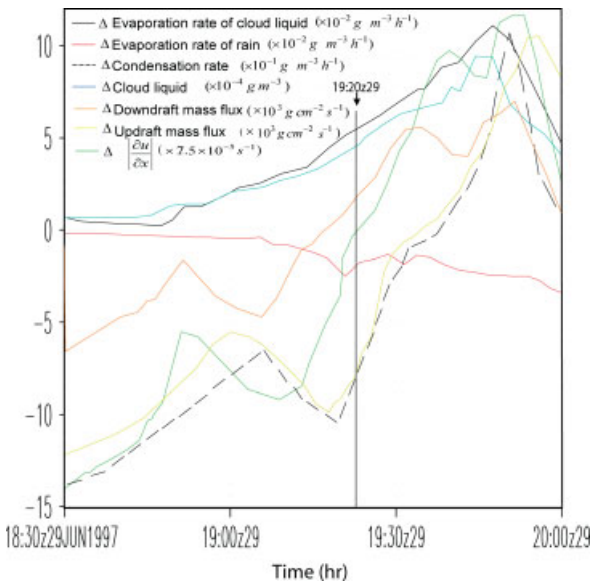

Figure 7. Time series of difference (high aerosol minus low aerosol) in domain-averaged evaporation rate of cloud liquid and rain ($\times 10^{-2}$ g m^{-3}h^{-1}), condensation rate ($\times 10^{-1}$ g m^{-3} h^{-1}), cloud liquid ($\times 10^{-4}$ g m^{-3}), updraught and downdraught mass fluxes ($\times 10^{3}$ g cm^{-2}s^{-1}), and $|\partial u/\partial x|$ ($\times 7.5 \times 10^{-5}$ s^{-1}) between 1830 and 2000 GMT on June 29. Downdraught mass flux and $|\partial u/\partial x|$ are averaged over the lowest 1 km.

lead the development of (first) increased downdraught mass fluxes and convergence and (finally) increased updraught mass fluxes and condensation, establishes causality.

Figure 10 shows time- and domain-averaged vertical profile of potential temperature up to 1920 GMT when the convergence becomes more intense at high aerosol. The high-aerosol run (Exp. 1) shows greater atmospheric instabilities, most of whose differences are present below the freezing level due to cooling from cloud-liquid evaporation. These greater instabilities at high aerosol indicate favourable conditions for stronger updraughts through the development of stronger downdraughts and low-level convergence.

Figures 11(a) and (b) are the superposition of vertically averaged evaporation rate and convergence at the surface at 1925 GMT, 5 minutes after the development of more intense near-surface convergence at high aerosol. Figures 8(c) and (d) show the distribution of evaporation and condensation rates and wind vectors at 1925 GMT. The locations of strong evaporation rates coincide closely with strong convergence and divergence (Figures 11(a) and (b)). Rain and cloud liquid which are transported from updraughts (low-level convergence) to unsaturated areas evaporate locally and generate proximate downdraughts (low-level divergence) as shown in Figures 8(c) and (d). Cloud liquid evaporates more readily than rain, and its greater abundance at high aerosol is associated with more extensive and stronger downdraught activity. Figures 8(e) and (f) show more intense convergence regions produce secondary cloud cells as simulated by Khain *et al.* (2005) at high aerosol at 1940 GTM, ~10 minutes before stronger updraughts and more condensation occur at high aerosol. However, secondary clouds are not formed in low-aerosol run (Exp. 3) due to weaker downdraughts leading to less intense convergence lines. Those secondary clouds at high aerosol contribute to increases in updraughts and thereby condensation,
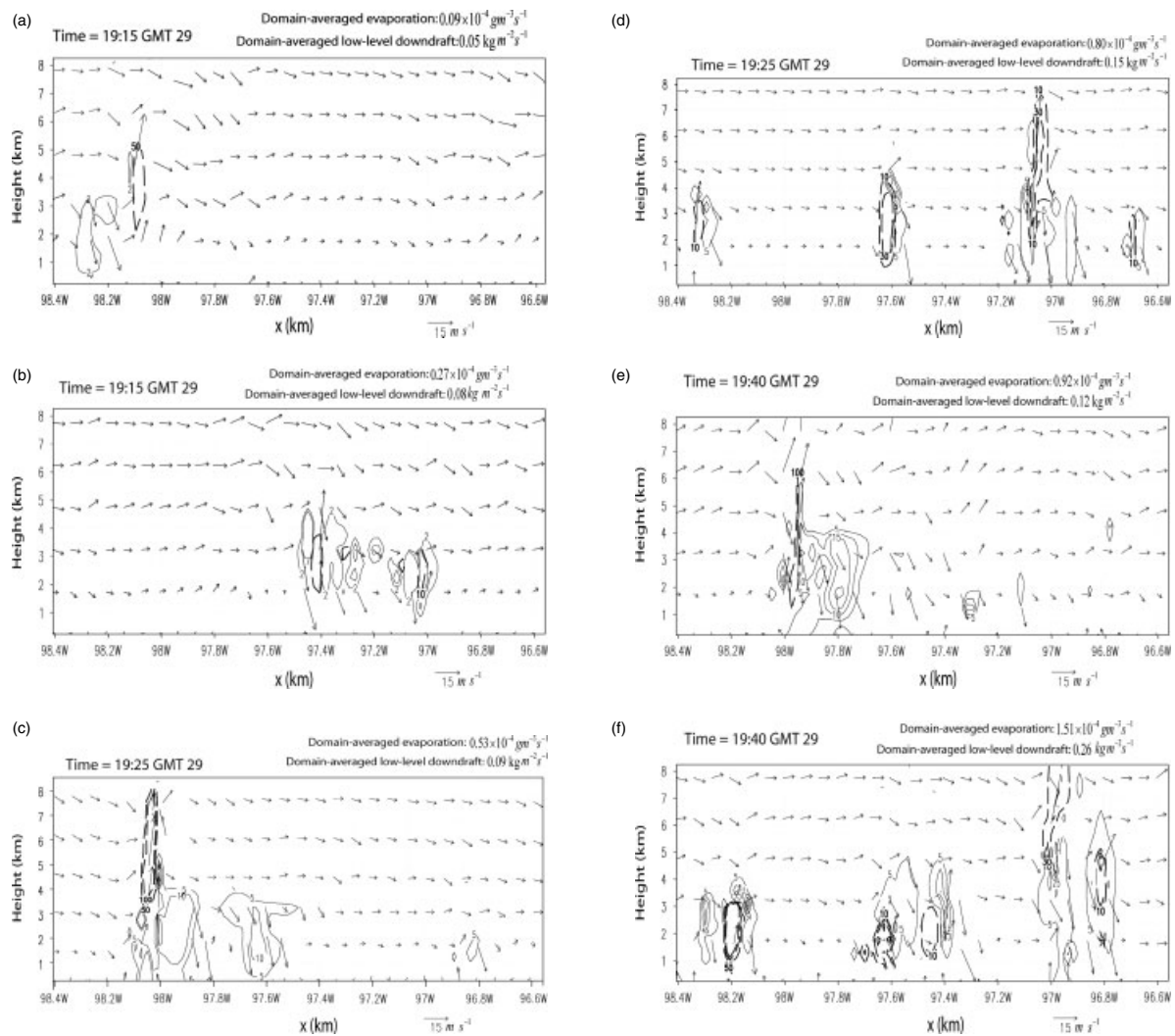
Figure 8. Wind vector fields (arrow) and contours of evaporation (solid line) and condensation (thick dashed line) rates. (a), (c), and (e) are for low-aerosol run (Exp. 3) and (b), (d), and (f) are for high-aerosol run (Exp. 1). For the effective visualization of interactions between vertical components of wind fields and latent heating/cooling, model-predicted vertical components of wind are multiplied by a factor of 10 and core regions of evaporation and condensation are displayed. For the display of the core regions, contour intervals and starting values vary from (a) to (f) as follows due to the large variation of evaporation and condensation among figures: *Condensation*: contour starting value: 50, 10, 50, 10, 100 and 10 ($\times 10^{-7}$ g m^{-3} s^{-1}); contour interval: 50, 50, 50, 20, 50 and 20 ($\times 10^{-7}$ g m^{-3} s^{-1}). *Evaporation*: contour starting value: 2, 2, 5, 5, 5 and 5 ($\times 10^{-7}$ g m^{-3} s^{-1}); contour interval: 5, 5, 5, 10, 5 and 20 ($\times 10^{-7}$ g m^{-3} s^{-1}).

leading to larger updraughts and condensation at high aerosol around 1950 GMT (Figure 7).

As time progresses, the population of clouds increases significantly at high aerosol through the development of more intense low-level convergence while the population of clouds does not change much at low aerosol, as shown in Figure 8. More clouds at high aerosol lead to more condensation and thus more precipitation. More clouds with more condensation result from more intense interactions between evaporation and downdraughts in convective clouds at the initial stage of time integration, leading to the formation of more intense low-level convergence at high aerosol than at low aerosol. This indicates the important role of those interactions in the initial clouds in the formation of secondary clouds and thus more precipitation at high aerosol.

As shown in Figure 8, the velocity of downdraughts around convective cells generally increases with decreasing

altitude, demonstrating that downdraughts accelerate as they descend. This indicates that hydrometeors in downdraughts evaporate, providing the source of negative buoyancy, and thus downdraughts here can be considered to follow moist-adiabatic descents, since downdraughts with no evaporation generally follow decelerating dry-adiabatic descents (Johnson, 1983). The temperature of descending parcels rise here, nearly following the moist adiabat. However, as parcels descend, the evaporation of hydrometeors in parcels keeps the temperature differences between parcels and ambient air large enough to accelerate downdraughts. More cooling from cloud-liquid evaporation keeps those temperature differences larger, resulting in more intense downdraughts at high aerosol than at low aerosol.

Due to delayed conversion of cloud liquid to rain, more cloud liquid is present at the beginning stage of cloud development in the high-aerosol run (Exp. 1) than

in the low-aerosol run (Exp. 3). More cloud liquid provides more abundant source of cloud-liquid evaporation, leading to more cooling from cloud-liquid evaporation in the high-aerosol run (Exp. 1). More cooling from cloud-liquid evaporation triggers stronger low-level convergence and updraughts in the high-aerosol run (Exp. 1) through the development of more intense downdraughts, which fosters the formation of secondary clouds and thus induces more condensation. Then, more condensation and delayed conversion of cloud liquid to rain both contribute to increased cloud liquid at high aerosol. This enables not only more collection of cloud liquid but also more transportation of cloud liquid to unsaturated areas (intensifying feedbacks among evaporation, downdraughts, low-level convergence, updraughts and further condensation), leading to more precipitation at high aerosol.

Based on Xu (1995), cloud systems are divided to convective and stratiform regions. The convective region includes a deep convective core and adjacent grid columns; grid columns whose centre is within 2 km of that of a core are within the convective region. A core satisfies at least one of the following three conditions: (1) maximum cloud up/downdraught strength, w_{max}, is larger than the average over grid columns
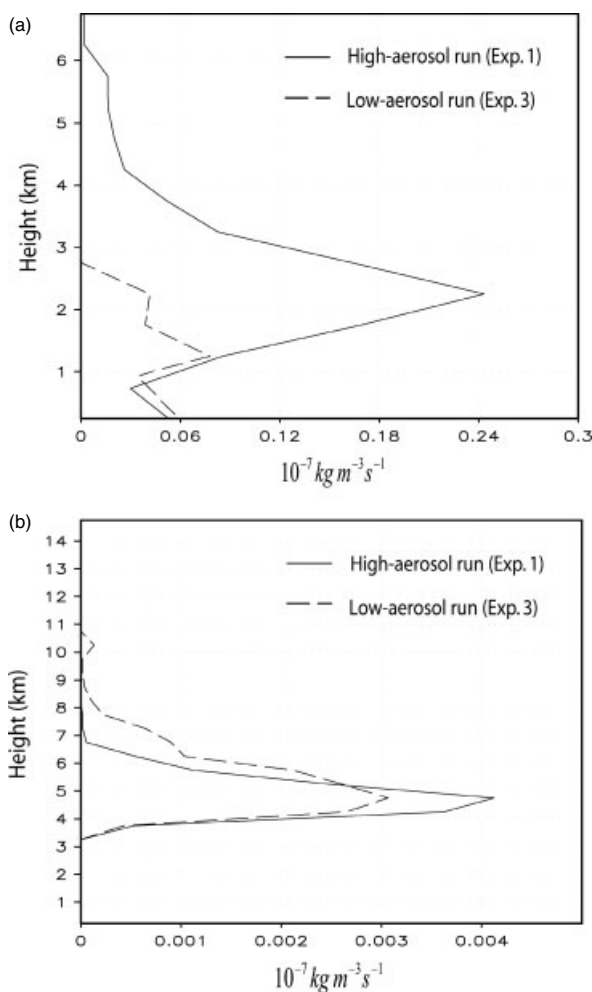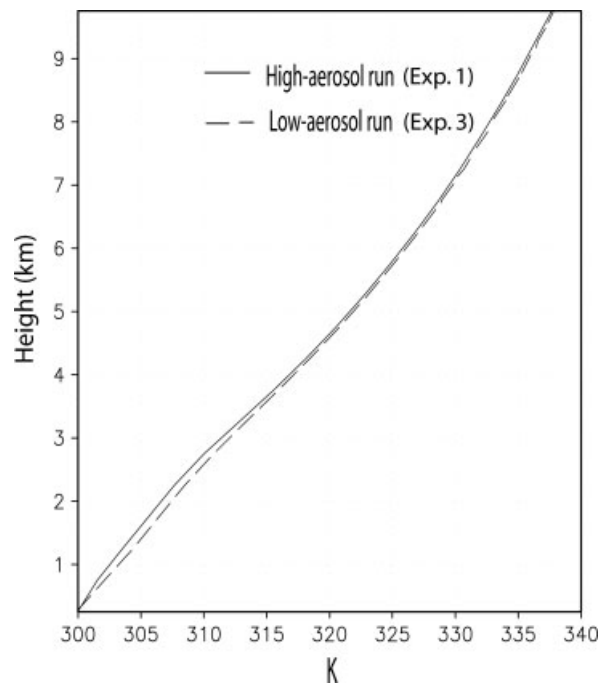

Figure 10. Vertical distribution of time- and domain-averaged potential temperature up to 1920 GMT on June 29.

within 4 km with $w > 1$ m s^{-1}, (2) $w_{max} > 3$ m s^{-1}, or (3) precipitation rate exceeds 25 mm h^{-1}. At high aerosol, cumulative precipitation in the stratiform region is smaller by 2.73 mm but, due to precipitation heavier by 8.05 mm in the convective region, cumulative precipitation is larger. Increasing aerosols suppress precipitation in the stratiform region due to weak interaction between dynamics and microphysics. The stronger updraughts leading to larger precipitation are convective. This indicates that the intensification of downdraughts in convective cells leads to increased precipitation at high aerosol. The intensification of mesoscale downdraughts in stratiform regions do not play a role in increased precipitation at high aerosol.

Ultimately, the increase in precipitation between high- and low-aerosol runs results from the dynamic response to evaporation of cloud liquid. Shallow cloud systems, with limited vertical extents over which downdraughts can develop, lack this positive feedback, without which reduced autoconversion and rain formation at high aerosol tend to decrease precipitation rates.

4.4. Effects of cold microphysics and radiation

Since ice particles have different properties (e.g. terminal velocity, particle density, latent heat associated with phase transition, saturation water vapour mixing ratio at a particular temperature) from those of liquid particles, their effects on aerosol-cloud interactions through microphysical processes must be different from those of liquid particles. Ice particles affect condensational growth of droplets above the freezing level through the Bergeron process. Also, processes such as collisions involving ice particles, homogeneous freezing of haze particles and
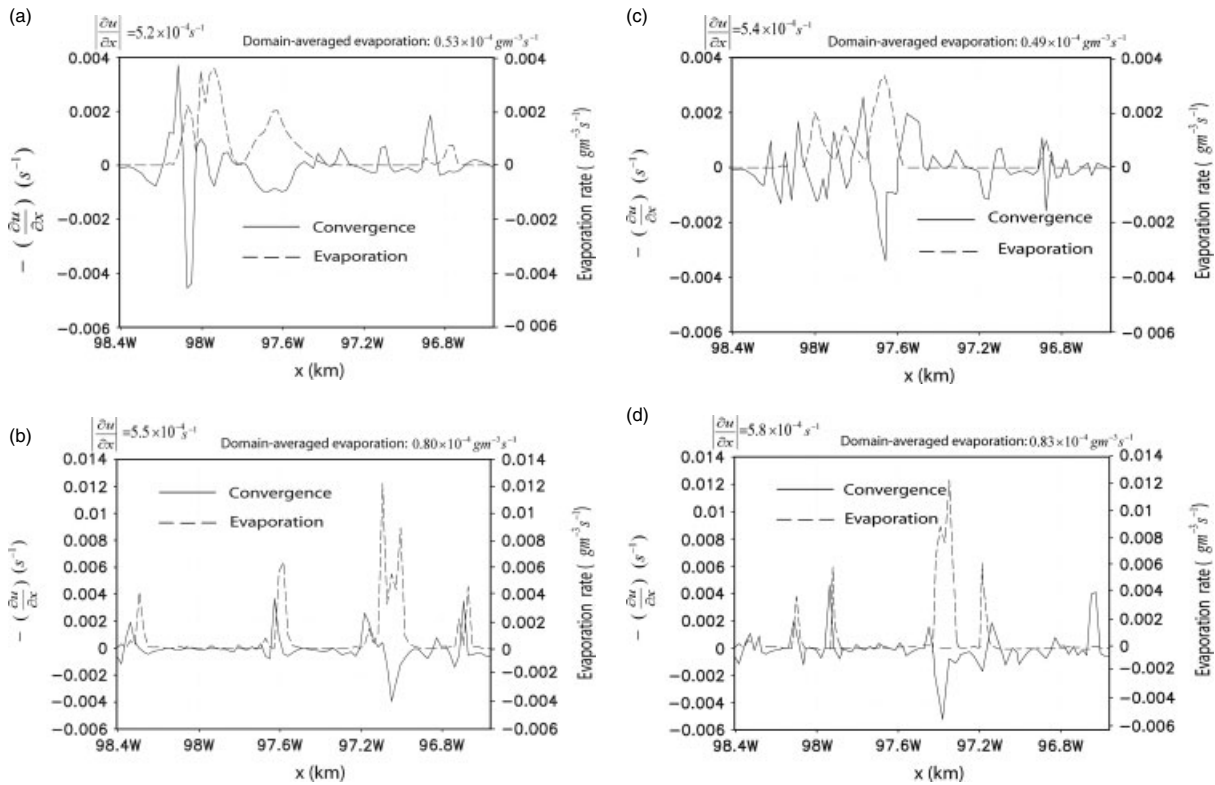

Figure 9. Vertical distribution of time- and domain-averaged (a) evaporation rate and (b) sublimation rate up to 1915 GMT on June 29.

Figure 11. Superposition of vertically averaged evaporation rate (g m^{-3} s^{-1}), and convergence field (s^{-1}) at the surface for (a) low-aerosol run (Exp. 3) and (b) high-aerosol run (Exp. 1) at 1925 GMT on 29 June, and (c) low-aerosol run (Exp. 2) and (d) high-aerosol run (Exp. 4) at 1915 GMT on 29 June.

droplets, Hallett and Mossop's ice-splintering and phase transitions of ice particles (i.e. deposition, sublimation, freezing, melting) can have significant impacts on ice particle number and mass. This in turn affects precipitation, and those processes change with increasing aerosols, since aerosols affect liquid-particle mass and number and most of those processes involve liquid particles as shown in the description of those processes in Tables II and III. Here, we examine the overall effects of those ice processes by performing another pair of experiments with the same conditions, except that the cold microphysics is turned off. The approximate difference equation (autoconversion – accretion form) of the precipitation budget in the absence of cold microphysics is as follows:

$$\Delta < \frac{\partial q_r}{\partial t} >= \Delta \| Pr \|$$

$$3.99$$

$$= \Delta < Au(q_r; q_c | q_c) > + \Delta < A(q_r; q_c | q_r) >$$

$$-17.42 \qquad 21.41 \quad (\text{mm}).$$

$$(8)$$

Autoconversion produces more rain at low aerosol, but accretion of cloud liquid by rain produces enough extra rain to overcome the deficit in autoconversion, which leads to more precipitation at high aerosol. The terms involving cloud liquid in (8) are replaced by the terms which balance them in the liquid-water budget to yield

the approximate condensation – evaporation form of the precipitation budget:

$$\Delta \| Pr \| = \Delta < C(q_c; q_v) > -\Delta < E(q_v; q_c) >$$

$$3.99 \qquad 29.17 \qquad 25.18 \quad (\text{mm}),$$

$$(9)$$

which indicates that larger precipitation at high aerosol is associated with larger condensation as in the cases including cold microphysics. Normalized precipitation with respect to condensation at high aerosol (0.32) is lower than that at low aerosol (0.38) at the end of time integration, indicating more intense dynamics at high aerosol.

Figure 5(c) shows the time series of the vertical average of $|\partial u/\partial x|$ over the horizontal domain and lowest 1 km for the runs with no cold microphysics. As in the runs with cold microphysics, the high aerosol run begins to show more active near-surface convergence around 1930 GMT. This results from larger evaporation at high aerosol, leading to stronger downdraught mass fluxes and more intense convergence. The stronger convergence field causes more intense updraught activity and more condensation. The resultant increased cloud liquid generates more rain as it is collected by rain.

The difference in precipitation is about 75% of that in the cases including cold microphysics. Cold microphysics increases the difference in precipitation. More active low-level convergence and thereby more precipitation at high aerosol are still simulated in the absence of ice

microphysics. This indicates the mechanism leading to heavier precipitation with increasing aerosols operates regardless of the presence of ice physics.

Mainly due to different amount of cloud liquid, net radiative heating rates are different between high- and low-aerosol runs as shown in Figure 12(b), depicting time- and domain-averaged net radiative heating after 1920 GMT when more intense low-level convergence begins to develop at high aerosol. Due to larger mass of cloud liquid at high aerosol, there is less and more cooling around the base and top of liquid cloud, respectively, at high aerosol. This may lead to greater instability for larger precipitation at high aerosol. However, radiative heating up to 1920 GMT, when more intense low-level convergence starts to develop at high aerosol, shows negligible differences between high- and low-aerosol runs (Figure 12(a)). After ~1920 GMT, due to more condensation led by more intense low-level convergence, cloud liquid at high aerosol becomes substantially larger than at low aerosol and this leads to larger differences in radiative heating, as shown in Figure 12(b). Hence, the key mechanisms leading to heavier precipitation with increasing aerosols begin to operate before significant differences in radiative heating rates occur, so the different radiative heating is not expected to change the qualitative nature of the results. To confirm this, experiments are repeated, removing radiation processes. They showed more intense low-level convergence and larger precipitation at high aerosol. The high-aerosol run shows 4.79 mm larger domain-averaged cumulative precipitation, which is ~90% of that in cases with radiation. Radiation increases the difference in precipitation, but interactions between dynamics and microphysics play crucial roles in the establishment of the key mechanisms for larger precipitation at high aerosol.

4.5. Runs with different initial conditions and other case-studies

The high-aerosol run (Exp. 4) shows ~17% larger precipitation than the low-aerosol run (Exp. 2) (Figures 3(d) and (e)) through the intensification of low-level convergence triggered by more evaporative cooling as observed in the Exp. 1 versus Exp. 3 pair with different initial conditions described above. Note that high-aerosol run (Exp. 4) adopts meteorological fields of low-aerosol run (Exp. 2) as initial fields (Table I). As shown in the following difference equation (high-aerosol run (Exp. 4) – low-aerosol run (Exp. 2)), the large increase in condensation leads to more precipitation in high-aerosol run (Exp. 4) despite lower precipitation efficiency. Normalized precipitation with respect to condensation in high-aerosol run (Exp. 4) (0.38) is lower than that in low-aerosol run (Exp. 2) (0.43) at the end of the time integration (Figure 3(f)).

$$\Delta \| Pr \| \approx \Delta < C(q_c; q_v) > - \Delta < E(q_v; q_c) >$$

$$5.01 \qquad 21.34 \qquad 16.84 \qquad (mm).$$

Figures 5(d) and (e) show the time series of the average of updraught mass flux and $|\partial u/\partial x|$ over the
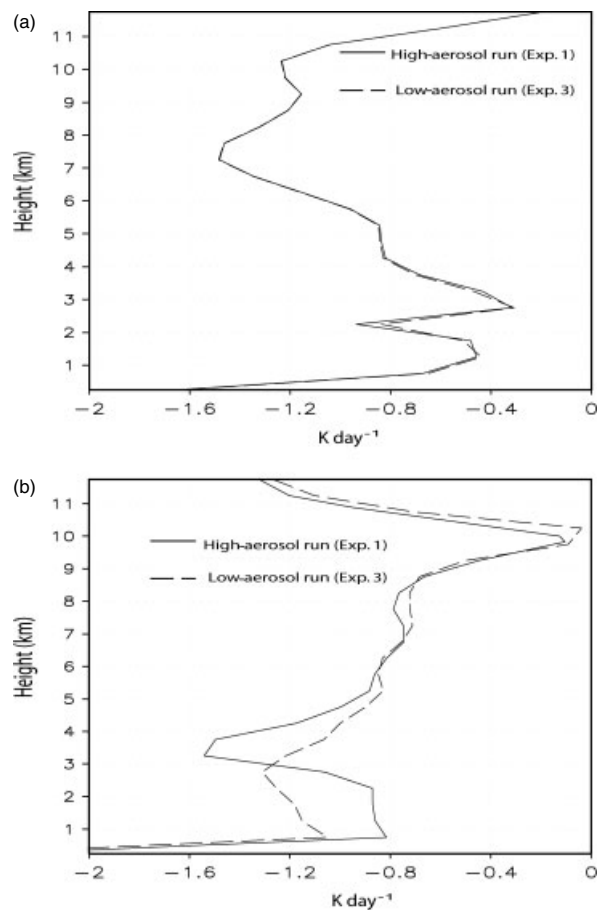

Figure 12. Vertical distribution of time- and domain-averaged net radiative heating rate (a) before and (b) after 1920 GMT on June 29.

horizontal domain and lowest 1 km, where u is the horizontal wind velocity. In high- aerosol run (Exp. 4), $|\partial u/\partial x|$ begins to exceed its value in low-aerosol run (Exp. 2) at 1910 GMT on 29 June, indicating more active near-surface horizontal convergence, leading to more intense updraughts around 1930 GMT (Figure 5d). Figures 11(c) and (d) are the superposition of vertically averaged evaporation rate and convergence at the surface at 1915 GMT, 5 minutes after the development of more intense near-surface convergence in high-aerosol run (Exp 4.). These figures indicate increased cloud liquid and evaporation at high aerosol drive stronger convergence at high aerosol. Due to stronger convergence at the surface at high aerosol, more intense updraughts and active condensation take place as shown in Figures 6(c) and (d) showing the superposition of vertically averaged condensation rate and convergence at the surface at 1935 GMT, 5 minutes after the updraught in high-aerosol run (Exp. 4) begins to be more intense than in low-aerosol run (Exp. 2). These indicate the mechanism identified in section 4.3 is robust to slightly varying initial meteorological conditions.

Based on results in this single case-study, it is difficult to draw a general conclusion that an increase of aerosol leads to an increase of precipitation in MCE via the intensification of deep convection. Establishing the generality

of the conclusion requires further investigation into more cases.

Two additional pairs of experiments are performed for sub-cases B and C of the ARM program. These are also MCE cases driven by deep convection. Comparisons between high- and low-aerosol runs in these sub-cases are based on simulations which are performed over the whole observation periods, 7–12 July 1997 for sub-case B and 12–17 July 1997 for sub-case C. The same CSRM and model set-up as for sub-case A are applied to these experiments, except that ARM sub-cases B and C observations provide large-scale forcing and surface fluxes, and background aerosol profiles are obtained on the beginning dates of sub-cases B and C.

The difference equations of precipitation for sub-cases B and C are obtained in the same manner as in the ARM sub-case A:

$$\Delta \|Pr\| \approx \Delta < C(q_c; q_v) > - \Delta < E(q_v; q_c) >$$

B :   3.63   20.23   17.05

C :   3.27   19.12   16.21

The budget numbers placed beneath the above equations indicate that the large increase in condensation leads to more precipitation at high aerosol, as in (7) and (9). ARM sub-cases B and C show 20% and 16% more precipitation at high aerosol despite lower precipitation efficiency. Precipitation efficiencies are 0.36 and 0.31 at high aerosol and 0.43 and 0.37 at low aerosol for sub-cases B and C, respectively. Figure 13 shows time series of domain-averaged low-level convergence of sub-cases B and C. High-aerosol runs develop more intense low-level convergence due to more evaporative cooling, leading to stronger updraught mass flux in convective regions as shown in Figure 14. Stronger updraughts at high aerosol lead to more condensation. At least for these three sub-cases, aerosols increase precipitation.

5. Summary and discussion

Enhanced aerosol concentrations for the ARM sub-cases of summer MCE studied here increase precipitation. This result is in marked contrast to the behaviour of stratiform clouds observed by Albrecht (1989), for which precipitation decrease is associated with high aerosol. Although autoconversion drops sharply as aerosol increases, compensating increases in collection of cloud liquid offset reduced autoconversion (Table II). This offset results from increased condensation at high aerosol, leading to increased precipitation at high aerosol (Table III). Increase in condensation, larger than increase in evaporation, led to a drier atmosphere at high aerosol than at low aerosol. The interaction between dynamics and microphysics in convective regions, in which increased evaporation resulting from much larger cloud liquid at high aerosol generates increased downdraught activity with interacting, converging outflows, is necessary for the increased precipitation. Stronger updraughts induced
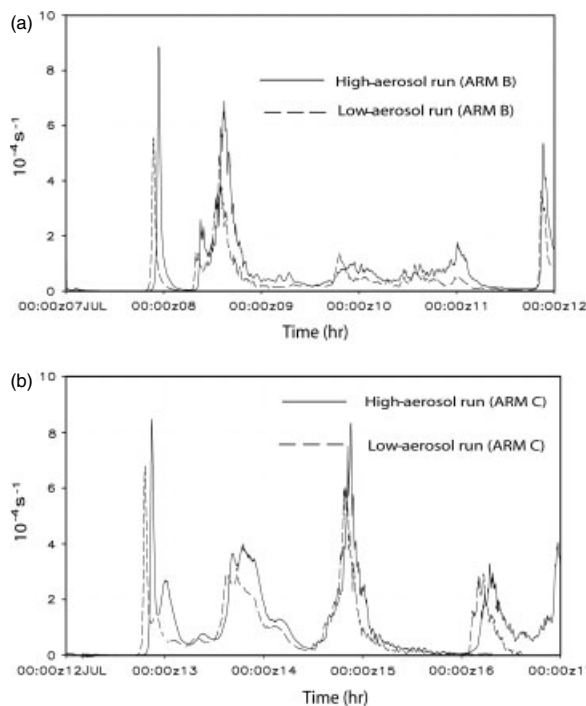

Figure 13. Time series of $|\partial u / \partial x|$ averaged over horizontal domain at the lowest 1 km, for ARM sub-cases (a) B and (b) C. u is horizontal wind velocity.
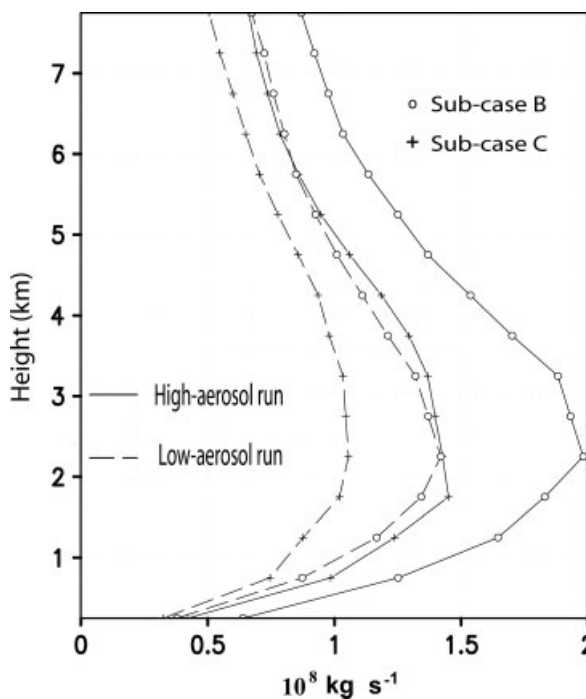

Figure 14. Vertical distribution of time-averaged updraught mass flux in convective regions for ARM sub-cases B and C.

by more intense low-level convergence produce larger condensation and, thereby, precipitation at high aerosol as shown in Figures 7 and 8. The formation of secondary clouds at high aerosol play a crucial role in more condensation and precipitation in MCE as simulated in the cases of a single cloud by Khain *et al.* (2005) (Figure 8(f)).

The absence of such a dynamic feedback in stratiform clouds blocks the increased precipitation mechanism at high aerosol, and the well-documented precipitation suppression at high aerosol results, noted by Albrecht (1989). Cold microphysics and radiative heating magnify the precipitation increase at high aerosol, but cold microphysics and radiation in this case, at least, are not essential to the precipitation increase.

Khain *et al.* (2004), Cui *et al.* (2006), Phillips *et al.* (2007b) and Khain *et al.* (2008) simulated the Texas, Cooperative Convective Precipitation Experiment (CCOPE) and Amazon cases of convective clouds. These cases showed less precipitation at high aerosol. Similar to this case, clouds in the Texas cases reached 14 to 15 km with vertical velocities exceeding 20 m s^{-1} and anvils of 100 km length. In the CCOPE case (Cui *et al.*, 2006), convection was less extensive than in this study with cloud tops at 10 to 11 km and vertical velocities exceeding 15 m s^{-1}. These studies indicate the mechanisms which increase precipitation with increasing aerosol in the cases of convective clouds in this study do not operate in all cases.

Cui *et al.*'s (2006) study indicated immersion freezing is most dominant among ice-nucleation paths and less vigorous near the top of clouds at their mature stages at high aerosol due to more rapid evaporation of smaller drops in the CCOPE case. This process reduced the buoyancy at cloud top and produced stronger downdraughts flanking the updraught core of the high-aerosol clouds, cutting off the inflow within the boundary layer to lead to weaker updraughts and less precipitation at high aerosol. Cui *et al.*'s (2006) study simulated clouds existing predominantly below the homogeneous freezing level whereas this study simulated clouds growing above the homogeneous freezing level. This study found greater homogeneous freezing of aerosol (haze) particles and droplets contributed to larger number and mass of ice crystals around the top of clouds at their mature stages, boosting the deposition and, thereby, buoyancy at high aerosol. Cui *et al.*'s (2006) study considered the case of weak wind shear. As simulated by Cui *et al.* (2006) and found by Weisman and Klemp (1982), when wind shear was weak, downdraughts destroyed the updraughts. However, in this study with moderate wind shear according to Bluestein's (1993) definition, downdraught regions were separated from updraught cores (Figure 8) to lead to the updraught-increasing mechanisms via the developments of stronger downdraughts and thereby low-level convergence at high aerosol.

In cumulus clouds in the CCOPE and Texas cases, the increase in condensation was less than that in evaporation, leading to precipitation suppression at high aerosol, as in the cases of cumulus and stratocumulus clouds with low CAPE and weak shear in Lee *et al.* (2008). But for deep convective clouds simulated here, due to moderate wind shear and large cloud vertical extent, evaporation of cloud liquid and development of downdraughts were more effective than those in cumulus clouds, leading to significantly increased condensation at high aerosol,

as shown in the deep convective cases in Lee *et al.* (2008) and squall line cases in Khain *et al.* (2005) and Lynn *et al.* (2005a,b). The extent of the precipitation-increasing interactions in these deep convective cases can be limited by other atmospheric characteristics. Humidity and boundary-layer properties can be additional factors to control the formation of precipitation-increasing secondary clouds (Khain *et al.*, 2008). If those factors act to limit the formation of precipitation-increasing secondary clouds, increased evaporation and sublimation will lead to reduced precipitation.

Bulk microphysics here divides liquid into cloud liquid and rain and this introduces autoconversion and accretion parametrizations to simulate the conversion of droplets to rain. The division of liquid into cloud liquid and rain introduces a spectral gap in the particle size distribution where, in reality, none exists. Cohard and Pinty (2000) indicated most differences in the evolution of drop-size distribution via collisions among drops between parametrizations and a bin model were in mid-size drops ($\sim$90 µm $<$ D $<$ $\sim$200 µm). However, as indicated by Cohard and Pinty (2000), drops in this mid-size range were to be collected by rain drops in the large-size range (D $>$ $\sim$200 µm) and, thereby, depleted rapidly to be a part of precipitating rain drops; once large rain drops formed, these discrepancies between parametrization and a bin model in the mid-size range disappeared quickly. Hence, the important thing is to predict correctly the onset of rain formation, which is done here in terms of the average droplet size reaching an observed threshold (20 µm). The justification for this is that autoconversion displays a threshold behaviour with respect to average droplet size (e.g. Tripoli and Cotton, 1980; Khairoutdinov and Kogan, 2000; Pawlowska and Brenguier, 2003).

Due to a computational burden, most CSRM studies of convective clouds adopt vertical grid resolutions whose order of magnitude is $\sim$100 m, as in this study. This is much larger than the depth of a layer over which the primary nucleation occurs. Hence, instead of simulating the nucleation processes explicitly as in parcel models, generally CSRM studies have relied on nucleation parametrizations. These parametrizations use vertical velocity, temperature, humidity and aerosol chemical and physical properties which are resolved on the model grid to calculate a maximum supersaturation in air parcels. In the real atmosphere, this maximum supersaturation is located only very close to ($\sim$10 m above) the cloud base itself and is a decisive factor determining the primary nucleation rate for the given aerosol properties. This maximum supersaturation is an equilibrium saturation when supersaturation production by updraughts is exactly balanced by supersaturation depletion by condensation in air parcels. Although the detailed processes, through which supersaturation reaches its equilibrium value by the balancing mechanism in rising air parcels, cannot be simulated explicitly with the CSRM resolution here, it is possible to calculate the equilibrium value using the resolved atmospheric conditions and aerosol

properties on the model grid. This calculation of equilibrium value generally adopts the assumption that vertical velocity does not vary during nucleation processes despite condensation in air parcels as in Ming *et al.*'s (2006) nucleation scheme used here. This assumption is supported by the fact that vertical velocity is not expected to vary widely in a layer of ∼10 m depth over which the nucleation occurs. That Ming *et al.*'s scheme showed a good agreement with results of parcel models as shown in Figure 1 in Ming *et al.* (2006) indicated the assumption works reasonably well. For the given atmospheric conditions and aerosol properties, Ming *et al.*'s scheme calculates condensation rate at the equilibrium state and, thereby, obtains the equilibrium supersaturation to calculate the nucleation rate. Although nucleation rate can be calculated reasonably by the parametrization compared with parcel-model results, 500 m resolution here limits the exact determination of locations of cloud bases. However, the uncertainty of the location of cloud bases within the 500 m layer is not likely to affect the qualitative nature of the results here, since the differences in evaporation in mid-level of clouds about 2–3 km above the bases play crucial roles in heavier precipitation at high aerosol.

Recent bin-model studies by Lynn *et al.* (2005a,b) and Khain *et al.* (2005) also simulated stronger near-surface convergence triggered by larger evaporation, leading to precipitation enhancement at high aerosol. More available cloud liquid for evaporation due to delayed autoconversion played a critical role in larger precipitation at high aerosol. CDNC in bin-model studies were predominantly determined by droplet nucleation. High and low CDNCs in bin-model studies were mostly caused by high and low aerosol numbers, resulting in high and low nucleation rates at high and low aerosol. This led to delayed autoconversion at high aerosol. Evolution of drop-size distribution in this study was not simulated as explicitly as in bin-model studies. Nonetheless, nucleation and autoconversion parametrizations were able to simulate similar CDNC differences for delayed autoconversion and thereby precipitation enhancement at high aerosol similar to those simulated in bin microphysics.

The choice of 2 km horizontal resolution affords substantial computational advantages. Convective cloud cell and its dynamics have been reported to be captured with 2 km resolution reasonably well. A series of test calculations with a similar cloud-system model with resolutions ranging from 500 m to 5 km showed that basic features of the simulations (e.g. patterns of vertical velocity) did not vary much for horizontal resolutions of 2 km or finer (Donner *et al.*, 1999). For shallower clouds, though, this resolution becomes more problematic. However, the intensification of low-level convergence and subsequent development of stronger updraughts for larger precipitation at high aerosol were convective as shown in section 4.3. In other words, the precipitation enhancement shown here was associated with the modification of dynamics in deep convective clouds, which were reasonably resolved by the resolution adopted here. The changes in

updraughts and downdraughts in convective cells due to aerosols were essential for heavier precipitation at high aerosol in this study, and those dynamical patterns were expected to be reasonably captured with 2 km resolution here, as reported by Donner *et al.* (1999).

Ekman *et al.* (2004, 2006) simulated deep convective clouds and aerosol physical and chemical properties reasonably well compared with observations using a CRM coupled with bulk microphysics with 2 km resolution. They used aerosol modules in their CRM coupled with bulk microphysics, taking into account physical and chemical processes of aerosols in detail, and found spatial redistributions of aerosols were strongly controlled by the vertical convective transport. Aerosol spatial retributions are important, since they predominantly determine spatial distributions of droplet nucleation for a given meteorological condition, strongly affecting CDNC and, thereby, autoconversion distributions. Those redistributions and, thereby CDNC distributions, showed a good agreement with observations, since updraughts and downdraughts were captured reasonably well, indicating the 2 km resolution can be used for the reasonable simulation of aerosol transport and CDNC spatial distributions. However, they indicated impaction scavenging (the removal of aerosols by precipitation) were able to reduce aerosols significantly, which could reduce aerosol differences, and thereby, cloud sensitivity to aerosols between high- and low-aerosol runs. (Note that this study considered nucleation scavenging only.) Impaction scavenging was most effective when clouds developed heavy precipitation at their mature stages (Ekman *et al.*, 2004, 2006). The key mechanisms leading to heavier precipitation with increasing aerosols began to operate before heavy precipitation developed (cf. Figures 3 and 5, which showed the domain-mean convergence magnitude increased before the onset of heavy precipitation), so the neglect of impaction scavenging is not expected to change the qualitative nature of the results.

As with the choice of 2 km horizontal resolution, use of a 2D, rather than a 3D approach affords substantial computational advantages. However, some aspects of the dynamics and microphysics differ in 2D and 3D models as noted by Phillips and Donner (2007a). Phillips and Donner (2007a) found that vertical velocities and mass fluxes in deep convective updraughts, and downdraught mass fluxes, were larger in 3D than in 2D. Downdraughts play an important role in the interactions between dynamics and microphysics described in this paper. Phillips and Donner's (2007a) results suggest this mechanism may have been underestimated in 2D. Conversely, Phillips and Donner (2007a) also found that weak convective clouds were more numerous in 2D. To the extent these clouds play a role, they may be overestimated in 2D. A 3D version of experiments has also been conducted for the same case of MCE as in this study. For those simulations, single-moment microphysics, similar to Phillips and Donner (2007a), was used. The high-aerosol run in this 3D framework exhibited behaviour relative to the low-aerosol run similar to that in a 2D framework in

this study with increased precipitation with increased precipitation (13%), increased evaporation (150%), and increased domain-mean convergence magnitude (11%). Although the microphysics is highly simplified in the 3D experiment relative to that used here, this result suggests that the qualitative character of the results is not a result of the use of 2D in these experiments.

Phillips and Donner (2007) compared results obtained by averaging an ensemble of 85 small (170 km) domains with a single large (4800 km) domain and found their statistical behaviours to be similar. This suggests that results here are unlikely to change appreciably with domain size. Also, most of spatial scales of low-level convergence in convective regions, a key process linking aerosol increases to subsequent development of convective clouds and precipitation enhancement, are much smaller than the domain size here. Figures 6 and 11 show low-level convergences directly associated with convective cells (where strong condensation and evaporation occur) have spatial scales of $\sim$10–30 km. Hence, interactions among downdraughts, low-level convergence and updraughts simulated in convective regions in this study are not expected to be affected by the domain boundary significantly. This indicates their changing behaviours with aerosol increases simulated here are expected to be fairly robust to domain size.

The identical surface fluxes from observation are prescribed for high- and low-aerosol runs. Therefore, surface fluxes do not contribute to different low-level convergence and precipitation. In this study, we focused on how aerosols affect clouds and precipitation for an identical observed net heat and moisture supplied to or removed from the domain by large-scale flow and surface fluxes. Although feedbacks from differences in clouds onto the large-scale flow and surface fluxes cannot be captured by this design, this isolates interactions between aerosols, microphysics, and local dynamics (e.g. convergence fields within the model domain with zero domain-mean average) and enables the identification of microphysics-aerosol interactions on the scale of cloud systems.

Small-scale entrainment and detrainment processes at cloud top play important roles in the evolution of shallow convective clouds such as warm cumulus and stratocumulus. Hence, high-resolution models such as a large-eddy simulation (LES) model have been used for the simulations of those clouds (Chlond and Wolkau, 2000; Stevens *et al.*, 2005; Stevens and Bretherton, 2006). With a model whose resolution is as coarse as that employed here, entrainment and detrainment processes cannot be well represented and, therefore, the quantitative details of the precipitation changes associated with changes in aerosol concentration in shallow clouds are of limited reality here. Conceding this, these experiments still demonstrate strong interactions between dynamics and microphysics in deep convective clouds made possible by the vertical extent of deep convection over which strong downdraughts develop for intense low-level convergence. The limited vertical extent of shallow clouds does not allow

the variation of evaporative cooling to affect dynamics effectively, leading to precipitation suppression. In shallow clouds, downdraughts do not develop as intense as shown in Figure 8, due to shorter distance between the level of evaporation and the surface. The shorter distances lead to less acceleration of downdraughts heading for the surface, reducing the differences in downdraughts around the surface and thereby in low-level convergence between high- and low-aerosol runs. Hence, condensation increases are not large enough to compensate for the reduction in autoconversion at high aerosol for smaller precipitation than at low aerosol as shown in Lee *et al.* (2008).

Appendix

Deposition nucleation at temperatures higher than $-40\,°C$

At temperatures between -30 and $-40\,°C$ and between -5 and $-30\,°C$, DeMott *et al.* (2003) and Meyers *et al.*'s (1992) parametrizations, multiplied by a scaling factor, are used for deposition nucleation, respectively. For temperatures between -30 and $-40\,°C$:

$$N_{IN} = 1000[\exp\{12.96(S_i - 1.1)\}]^{0.3} \times \Psi \qquad (A.1)$$

Here, N_{IN} (m^{-3}) is ice-crystal number concentration, S_i the saturation ratio with respect to ice and Ψ a scaling factor to take into account the dependence of IN activation on dust mass. $\Psi = DU_{2.5}/DU_{2.5}^*$, where $DU_{2.5}$ is mass concentration of dust particles with diameter less than 2.5 μm and $DU_{2.5}^*$ is a reference dust mass concentration. $DU_{2.5}^*$ is set at 0.11 μg m^{-3} based on dust data from the Mount Werner project used to derive (A.1) (DeMott *et al.*, 2003). Hence, (A.1) computes N_{IN} based on variation of dust mass relative to dust mass observed at the Mount Werner project. It was observed that IN concentrations were almost linear with the concentrations of large aerosol particles (Georgii and Kleinjung, 1967; Berezinskiy *et al.*, 1986), supporting the assumption that N_{IN} is proportional to $DU_{2.5}^*$. For temperatures between -5 and $-30\,°C$, the same scaling factor as used in (A.1) is applied to Meyers *et al.*'s (1992) parametrization as

follows, since dust mass data are not available in Meyers *et al.* (1992):

$$N_{IN} = 63 \exp\{12.96(S_i - 1) - 0.639\} \times \Psi. \quad \text{(A.2)}$$

References

Albrecht BA. 1989. Aerosols, cloud microphysics, and fractional cloudiness. *Science* **245**: 1227–1230.

Bluestein HB. 1993. *Synoptic-dynamic meteorology in midlatitudes. Volume II: Observations and theory of weather systems.* Oxford University Press: Oxford, UK.

Chin M, Ginoux P, Kinne S, Torres O, Holben BN, Duncan BN, Martin RV, Logan JA, Higurashi A, Nakajima T. 2002. Tropospheric aerosol optical thickness from the GOCART model and comparisons with satellite and sun photometer measurements. *J. Atmos. Sci.* **59**: 441–460.

Chlond A, Wolkau A. 2000. Large-eddy simulation of nocturnal stratocumulus topped marine atmospheric boundary layer: An uncertainty analysis. *Boundary-Layer Meteorol.* **95**: 31–35.

Cohard J-M, Pinty J-P. 2000. A comprehensive two-moment warm microphysical bulk scheme. I: Description and tests. *Q. J. R. Meteorol. Soc.* **125**: 425–439.

Cui Z, Carslaw KS, Yin Y, Davies S. 2006. A numerical study of aerosol effects on the dynamics and microphysics of a deep convective clouds in a continental environment. *J. Geophys. Res.* **111**: DOI:10.1029/2002JD002911.

DeMott PJ, Cziczo DJ, Prenni AJ, Murphy DM, Kreidenweis SM, Thomson DS, Borys R, Rogers DC. 2003. Measurements of the concentration and composition of nuclei for cirrus formation. *Proc. Natl. Acad. Sci. USA* **100**: 14655–14660.

Donner LJ, Seman CJ, Hemler RS. 1999. Three-dimensional cloud-system modeling of GATE convection. *J. Atmos. Sci.* **56**: 1885–1912.

Ekman AML, Wang C, Wilson J, Ström J. 2004. Explicit simulations of aerosol physics in a cloud-resolving model: A sensitivity study based on an observed convective cloud. *Atmos. Chem. Phys.* **4**: 773–791.

Ekman AML, Wang C, Wilson J, Ström J, Krejci R. 2006. Explicit simulation of aerosol physics in a cloud-resolving model: Aerosol transport and processing in the free troposphere. *J. Atmos. Sci.* **63**: 682–696.

Facchini MC, Mircea M, Fuzzi S, Charlson RJ. 1999. Cloud albedo enhancement by surface-active organic solutes in growing droplets. *Nature* **401**: 257–259.

Field PR, Möhler O, Connolly P, Krämer M, Cotton R, Heymsfield AJ, Saathoff H, Schnaiter M. 2006. Some ice nucleation characteristics of Asian and Saharan desert dust. *Atmos. Chem. Phys.* **6**: 2991–3006.

Freidenreich SM, Ramaswamy V. 1999. A new multiple-band solar radiative parameterization for general circulation models. *J. Geophys. Res.* **104**: 31389–31410.

Grabowski WW, Wu X, Moncrieff MW. 1996. Cloud-resolving modeling of tropical cloud systems during phase III of GATE. Part I: Two-dimensional experiments. *J. Atmos. Sci.* **53**: 3684–3709.

Grabowski WW. 2006. Indirect impact of atmospheric aerosols in idealized simulations of convective–radiative quasi-equilibrium. *J. Climate* **18**: 4664–4682.

Hallett J, Mossop SC. 1974. Production of secondary ice particles during the riming process. *Nature* **249**: 26–28.

Hansen J, Sato M, Ruedy R. 1997. Radiative forcing and climate response. *J. Geophys. Res.* **102**: 6831–6864.

Hong S-Y, Pan H-L. 1996. Nonlocal boundary-layer vertical diffusion in a medium-range forecast model. *Mon. Weather Rev.* **124**: 2322–2339.

Hong S-Y, Noh Y, Dudhia J. 2006. A new vertical diffusion package with an explicit treatment of entrainment processes. *J. Atmos. Sci.* **24**: 2318–2341.

Houze RA. 1993. *Cloud dynamics*. Academic Press.

Johnson BC. 1983. The heat burst of 29 May 1976. *Mon. Weather Rev.* **111**: 1776–1792.

Khain A, Rosenfeld D, Pokrovsky A. 2003. Simulations of aerosol effects on convective clouds developed under continental and maritime conditions. *Geophys. Res. Abstr.* **5**: 03180.

Khain A, Pokrovsky A, Pinsky M, Seifert A, Phillips V. 2004. Simulation of effects of atmospheric aerosols on deep turbulent convective clouds using a spectral microphysics mixed-phase

cumulus cloud model. Part I: Model description and possible applications. *J. Atmos. Sci.* **15**: 2963–2982.

Khain A, Rosenfeld D, Pokrovsky A. 2005. Aerosol impact on the dynamics and microphysics of deep convective clouds. *Q. J. R. Meteorol. Soc.* **131**: 2639–2663.

Khain A, BenMoshe N, Pokrovsky A. 2008. Factors determining the impact of aerosols on surface precipitation from clouds: An attempt at classification. *J. Atmos. Sci.* **65**: 1721–1748.

Khairoutdinov M, Kogan M. 2000. A new cloud physics parameterization in a large-eddy simulation model of marine stratocumulus. *Mon. Weather Rev.* **128**: 229–243.

Klemp JB, Skamarock WC, Dudhia J. 2007. Conservative split-explicit time integration methods for the compressible non-hydrostatic equations. *Mon. Weather Rev.* **135**: 2897–2913.

Koch D, Rind D. 1998. Beryllium 10/beryllium 7 as a tracer of stratospheric transport. *J. Geophys. Res.* **103**: 3907–3918.

Krueger SK, Cederwall RT, Xie SC, Yio JJ. 1999. 'GCSS Working Group 4 Model Intercomparison – Procedures for Case 3: Summer 1997 ARM SCM IOP. Technical report obtainable from http://www.arm.gov/docs/scm/scmic3.

Leaitch WR, Strapp JW, Isaac GA. 1986. Cloud droplet nucleation and cloud scavenging of aerosol sulfate in polluted atmosphere. *Tellus* **38B**: 328–344.

Lee SS, Donner LJ, Phillips VTJ, Ming Y. 2008. The dependence of aerosol effects on clouds and precipitation on cloud-system organization, shear and stability. *J. Geophys. Res.* in press, DOI:10.1029/2007JD009224.

Lin YL, Farley RD, Orville HD. 1983. Bulk parameterization of the snow field in a cloud model. *J. Appl. Meteorol.* **19**: 1065–1092.

Lohmann U, Diehl U. 2006. Sensitivity studies of the importance of dust ice nuclei for the indirect aerosol effect on stratiform mixed-phase clouds. *J. Atmos. Sci.* **63**: 968–982.

Lynn BH, Khain AP, Dudhia J, Rosenfeld D, Pokrovsky A, Seifert A. 2005a. Spectral (bin) microphysics coupled with a mesoscale model (MM5). Part I: Model description and first results. *Mon. Weather Rev.* **133**: 44–58.

Lynn BH, Khain AP, Dudhia J, Rosenfeld D, Pokrovsky A, Seifert A. 2005b. Spectral (bin) microphysics coupled with a mesoscale model (MM5). Part II: Simulation of a CaPE rain event with a squall line. *Mon. Weather Rev.* **133**: 59–71.

Meyers MP, DeMott PJ, Cotton WR. 1992. New primary ice-nulceation parameterization in an explicit cloud model. *J. Appl. Meteorol.* **31**: 708–720.

Ming Y, Ramaswamy V, Donner LJ, Phillips VTJ. 2006. A new parameterization of cloud droplet activation applicable to general circulation models. *J. Atmos. Sci.* **63**: 1348–1356.

Möhler O, Field PR, Connolly P, Benz S, Saathoff H, Schnaiter M, Wagner R, Cotton R, Krämer M, Mangold A, Heymsfield AJ. 2006. Efficiency of the deposition mode ice nucleation on mineral dust particles. *Atmos. Chem. Phys.* **6**: 3007–3021.

Pawlowska H, Brenguier J-L. 2003. An observational study of drizzle formation in stratocumulus clouds for general circulation model (GCM) parameterization. *J. Geophys.Res.* **108**(D15): 8630, DOI:10.1029/2002JD002679.

Phillips VTJ, Donner LJ. 2007. Cloud microphysics, radiation, and vertical velocities in two- and three-dimensional simulations of deep convection. *Q. J. R. Meteorol. Soc.* **133**: 3011–3033.

Phillips VTJ, Donner LJ, Garner S. 2007a. Nucleation processes in deep convection simulated by a cloud-system-resolving model with double-moment bulk microphysics. *J. Atmos. Sci.* **64**: 738–761.

Phillips VTJ, Pokrovsky A, Khain A. 2007b. The influence of time-dependent melting on the dynamics and precipitation production in maritime and continental storm clouds. *J. Atmos. Sci.* **64**: 338–359.

Saleeby SM, Cotton WR. 2004. A large-droplet mode and prognostic number concentration of cloud droplets in the Colorado State University regional atmospheric modeling system (RAMS). Part I: Module description and supercell test simulations. *J. Appl. Meteorol.* **43**: 182–195.

Schwarzkopf MD, Ramaswamy V. 1999. Radiative effects of CH_4, N_2O, halocarbons and the foreign-broadened H_2O continuum: A GCM experiment. *J. Geophys. Res.* **104**: (D8) 9467–9488.

Seinfeld JH, Pandis SN. 1998. *Atmospheric chemistry and physics: From air pollution to climate change*. John Wiley & Sons.

Skamarock WC, Klemp JB, Dudhia J, Gill DO, Barker DM, Wang W, Powers JG. 2005. 'A description of the Advanced Research WRF Version 2'. Tech. Note NCAR/TN-468 +STR. NCAR: Boulder, USA. Available from http://www.mmm.ucar.edu/wrf/users/doc/arw_v2.pdf.

Stevens DE, Bretherton CS. 2006. Effects of resolution on the simulation of stratocumulus entrainment. *Q. J. R. Meteorol. Soc.* **125**: 425–439.

Stevens B, Moeng C-H, Ackerman AS, Bretherton CS, Chlond A, de Roode S, Edwards J, Golaz J-C, Jiang H, Khairoutdinov M, Kirkpatrick MP, Lewellen DC, Lock A, Müller F, Stevens DE, Whelan E, Zhu P. 2005. Evaluation of large-eddy simulations via observations of nocturnal marine stratocumulus. *Mon. Weather Rev.* **133**: 1443–1462.

Timmreck C, Schulz M. 2004. Significant dust simulation differences in nudged and climatological operation mode of the AGCM ECHAM. *J. Geophys. Res.* **109**: DOI:10.1029/2003JD004381.

Tripoli GJ, Cotton WR. 1980. A numerical investigation of several factors contributing to the observed variable intensity of deep convection over south Florida. *J. Appl. Meteorol.* **19**: 1037–1063.

van den Heever SC, Cotton WR. 2004. 'The impacts of Saharan dust on Florida convection'. Proceedings of 14th ICCP/IAMAS international conference on clouds and precipitation, Bologna, Italy, 18–23 July.

Wang C. 2004. A modeling study on the climate impacts of black carbon aerosols. *J. Geophys. Res.* **109**(D03106): DOI:10.1029/2003JD004084.

Weisman ML, Klemp JB. 1982. The dependence of numerically simulated convective storms on vertical wind shear and buoyancy. *Mon. Weather Rev.* **110**: 504–520.

Whitby KT. 1978. The physical characteristics of sulfur aerosols. *Atmos. Environ.* **12**: 135–159.

Xu K-M. 1995. Partitioning mass, heat and moisture budgets of explicitly simulated cumulus ensembles into convective and stratiform components. *J. Atmos. Sci.* **52**: 551–573.

Xu K-M, Cederwall RT, Donner LJ, Grabowski WW, Guichard F, Johnson DE, Khairoutdinov M, Krueger SK, Petch JC, Randall DA, Seman CJ, Tao W-K, Wang D, Xie SC, Yio JJ, Zhang M-H. 2002. An intercomparison of cloud-resolving models with the Atmospheric Radiation Measurement summer 1997 Intensive Observation Period data. *Q. J. R. Meteorol. Soc.* **128**: 593–624.

Zhang MH, Lin JL. 1997. Contrained variational analysis of sounding data based on column-integrated budgets of mass, heat, moisture and momentum: Approach and application to ARM measurement. *J. Atmos. Sci.* **54**: 1503–1524.

Zhang MH, Lin JL, Cederwall RR, Yio JJ, Xie SC. 2001. Objective analysis of ARM IOP data: Method and sensitivity. *Mon. Weather Rev.* **129**: 295–311.